NTNU

Norwegian University of
Science and Technology

Computational fluid dynamics simulations of a Formula Student race car

Effects predicted by the modelling of a steady state cornering vehicle

Kristian Forfot Sagmo

Master of Science in Physics and Mathematics
Submission date: September 2016
Supervisor: Jon Andreas Støvneng, IFY
Co-supervisor: Lars Roar Sætran, EPT

Norwegian University of Science and Technology
Department of Physics

NORWEGIAN UNIVERSITY OF SCIENCE AND TECHNOLOGY

Computational fluid dynamics simulations of a Formula Student race car - Effects predicted by the modelling of a steady state cornering vehicle

by

Kristian F Sagmo

A thesis submitted in partial fulfillment for the
degree of Master of Science

in the
Faculty of Natural Sciences and Technology
Department of Physics

September 2016

Preface

Throughout the last year, working with design and production of the aerodynamic devices implemented on the Revolve NTNU race-car Gnist, I've learned a lot regarding aerodynamics, compared to my starting point. I feel fortunate to have the opportunity as a student at NTNU to participate on such both fun and challenging engineering problems as building a car from scratch. I think it is especially good for the university student community, to be able to indulge in such projects along side the normal academic progression. Hence, I would like to thank the university administration for supporting such student communities.

Also, I would like to thank the team in Revolve NTNU. Without them, this work would not have been possible. Thanks also to my supervisors Lars Sætran, and Jon Andreas Støvneng, for both supporting and guiding me in this work. Especially thanks to Jan Bartl, for helping with and supervising the wind tunnel tests conducted, as well as providing fruitful discussions on the experiments regarding the NRELs826 airfoil.

Problem description

As a member of the 2016 Revolve NTNU team the task presented is two-fold:

First, using the CFD software package StarCCM+, evaluate the accuracy of RANS steady state simulations with respect to predicting aerodynamic forces on the 2016 race car Gnist. Investigate different cases of geometry of varying complexity, and compare with experimental reference cases. If time, compare simulation predictions with on track measurements.

Second, investigate the aerodynamic effects for a turning Formula Student vehicle, to see if significant discrepancies exists with respect to yaw cases.

Abstract

In this thesis work an investigation of the aerodynamics of a Fomula Student race car was conducted. The work focused on a computational fluid dynamics evaluation of the aerodynamic effects predicted for the car moving through relatively sharp corners of constant curvature. To assess the credibility of the closure models investigated, comparisons with experimental reference cases were conducted. To put some bounds on the numerical discretization errors for the car simulations, a grid convergence study was also conducted. For the simplified wing validation test cases, a relatively good agreement between aerodynamic performance values obtained from experiments and simulations was found. For the full car simulations, comparisons were made with on track measured values of lift. With respect to the measured values, the predictions of lift obtained from the simplified computer model geometry was high. It is believed that this was due, in part, to the simplicity of the model geometry, allowing for less disturbed air flow around the lift generating devices of the car, as well as the turbulence models inability to accurately predict amplitudes and the stream wise extent of the wake of bluff bodies directly upstream of several key lift generating devices. For assessing the aerodynamic effects of steady state cornering for the vehicle the momenta about its yaw, pitch and roll axes were tracked. In addition, lift, drag and sideforces were investigated. The modelling of rotational flow around the car found effects not present in, and in direct opposition to those predicted by modeling a cornering vehicle as having a fixed yaw angle with respect to the free stream.

Sammendrag

I dette arbeidet ble det foretatt en undersøkelse av aerodynamiske effekter på en Formula Student racer bil. Arbeidet fokuserte på numeriske strømnings beregninger for å evaluere aerodynamiske effekter som oppstår for en slik bil når den kjører gjennom relativt skarpe svinger med konstant kurvatur. For å evaluere nøyaktigheten til de numeriske modellene brukt i studiet ble det satt opp sammmenligninger med eksperimentelle referanse studier. For å estimere feil på grunn av diskretisering ble det foretatt en studie av gitter konvergens. I udersøkelsene av relativt enkle vinge geometrier ble det funnet en god korrelasjon mellom simulerte og målte verdier. For å vurdere nøyaktigheten av de numeriske modellene med hensyn på modellering av hele bilen ble det foretatt bane målinger. I forhold til de målte verdiene, estimerte de numeriske modellene basert på en forenklet geometrisk modell høye verdier. Dette anntaes å skyldes, blant annet, forenklingene av bil geometrien som gir renere luft til vingene på bilen, samt unøyaktiheten i turbulensmodellene. For å evaluere aerodynamiske effekter hos en bil i sving ble dreiemomenter om bilens akser beregnet, samt totalkrefter. Modelleringen av roterende luft omkring bilen forutså effekter som ikke opptredde ved bare å vinkle bilen relativt til fartsretningen.

Contents

List of Figures

List of Tables

Nomenclature

F_z	normal force	N
F_y	lateral force	N
F_x	longitudinal force	N
A_{ref}	frontal reference area	m^2
m	mass, vehicle mass	kg
g	gravitational acceleration, 9.815	ms^{-2}
h	ground height	m
c	chord length	m
DF	down-force	N
L	aerodynamic lift	N
S	aerodynamic side force	N
D	aerodynamic drag	N
r	turn radius	m
C_l	lift coefficient	
C_d	drag coefficient	
Re	reynolds number	
y^+	non-dimensional normal cell wall distance	
u^+	non-dimensional laminar boundary layer velocity	
GCI	grid convergence indicator	
CI	corner index, length/r	
p_{num}	order of numerical scheme	
U, V, W	mean flow velocity components	ms^{-1}
P	mean pressure	Nm^{-2}
u', v', w'	fluctuating velocity components	ms^{-1}
$\tilde{U}, \tilde{V}, \tilde{W}$	mean flow velocity components	ms^{-1}
$\tilde{\mathbf{U}}$	density weighted mean flow velocity vector	ms^{-1}
$\bar{P}$	time averaged pressure	Nm^{-2}
$S_{M_x}, S_{M_y}, S_{M_z}$	momentum source terms	
S_Φ	scalar flow variable source term	
$\overline{\bar{\rho}u'^2}$, $\overline{\bar{\rho}u'v'}$, $\overline{\bar{\rho}u'w'}$,		

$\overline{\bar{\rho}v'^2}$, $\overline{\bar{\rho}v'w'}$, $\overline{\bar{\rho}w'^2}$	Reynolds stress components	Nm^{-2}
$f_{\nu 1}$	wall damping function	
k	turbulent kinetic energy	Jkg^{-1}
$\triangle_{CPU}$	CPU iteration solver time	s
$\#_{tot}$	total cell count	
y^+_{max}	maximum y^+ value	
Y_m	yawing moment	Nm
P_m	pitching moment	Nm
R_m	rolling moment	Nm
ω	angular frequency	$\mathrm{rad{\cdot}s}^{-1}$
μ_f	friction coefficient	
ρ	density	kgm^{-3}
Φ	mean flow scalar quantity	
ϕ'	fluctuating scalar flow quantity	
$\bar{\rho}$	time averaged density	kgm^{-3}
$\tilde{\Phi}$	scalar density weighted mean flow variable	
Γ_Φ	scalar variable diffusion coefficient	
$\tilde{\nu}$	kinematic eddy viscosity	$\mathrm{m}^2\mathrm{s}^{-1}$
μ_t	turbulent viscosity, eddy viscosity	Pa·s
δ_{ij}	Kronecker delta	

CFD	**C**omputational **F**luid **D**ynamics
RANS	**R**eynolds **A**veraged **N**avier **S**tokes
SST	**S**hear **S**tress **T**ransport
SIMPLE	**S**emi - **I**mplicit **M**ethod for **P**ressure **L**inked **E**quations
FS	**F**ormula **S**tudent
DNS	**D**irect **N**umerical **S**imulation
2D	**2 D**imensional
3D	**3 D**imensional
CPU	**C**entral **P**rocessing **U**nit
RAM	**R**andom **A**ccess **M**emory

Chapter 1

Introduction

In the following a brief description of the Formula Student engineering competition is given. A general look at race-car aerodynamics follows, with an explanation and motivation of the objective of this study. Lastly, the conceptual approach and reasoning for using Computational Fluid Dynamics as an analysis tool is presented.

1.1 Formula Student racing

Formula Student is an engineering competition for university students organized by the International Institution of Mechanical Engineers in Europe and the Society of Automobile engineers in America. It is arguably the worlds largest university student competition, and takes place at different race-track venues around the globe. Students from a wide range of engineering fields cooperate in the university teams. Each year the teams are requested to design and build a single-seat race-car from scratch. Every team has just one year to go from nothing, to a fully assembled and thoroughly tested vehicle, built within the regulations stated in the competition "formula". Revolve NTNU is the university team representing NTNU in this competition. A photo of the race-car developed by the team for the 2016 season can be seen in figure 1.1.

In general for Formula Student racing the tracks are set up using cones and the track width is quite narrow compared to a car's width so that the the radii of the corners are relatively close to the path the center of the car follows around a circuit. A figure illustrating a typical track layout is given in figure 1.2. A few corner radii are indicated. The cars rarely utilize full engine power due to the large amount of relatively sharp turns. Instead, lateral grip is the main limiting factor. This has induced the FS community to do research on and take advantage of aerodynamic devices [1–3], even though average track speeds are quite low.

FIGURE 1.1: A picture of the Revolve NTNU 2016 race-car "Gnist" competing at the Formula Student event at Hockenheimring in Germany. Photo courtesy of Revolve NTNU.

Indeed, a study of the participating FS community reveals an increase in the use of aerodynamic devices by the teams over the recent years. While there still exists a relatively large variation in the forms of the aerodynamic devices employed, most packages now include such devices as a front wing, rear wing, and under body diffusers. An illustration of the devices implemented on the 2016 Revolve NTNU car, serving as the base geometric model for this study, is shown in figure 1.3.

1.2 The cornering condition

Traditionally a turning car is modelled as having a yaw angle with respect to the direction of heading [4]. For a car traveling through stationary air, the yaw angle is equal to the vehicle slip angle, later defined. Intuitively, one might argue that this approach should give a fair approximation of the case of a turning car, as long as the curved path assumed through the corner has a small degree of curvature compared to the vehicle slip angle. Let us for simplicity define a corner index for a car, as it's total length dived by the radius of the curved path it assumes, $CI = length/r$. From the illustration in figure 1.2 then, it is clear that for a Formula Student car with a CI approaching a minimum of 0.5, a degree of curvature of roughly 30 degrees is achieved at the sharpest corners. For

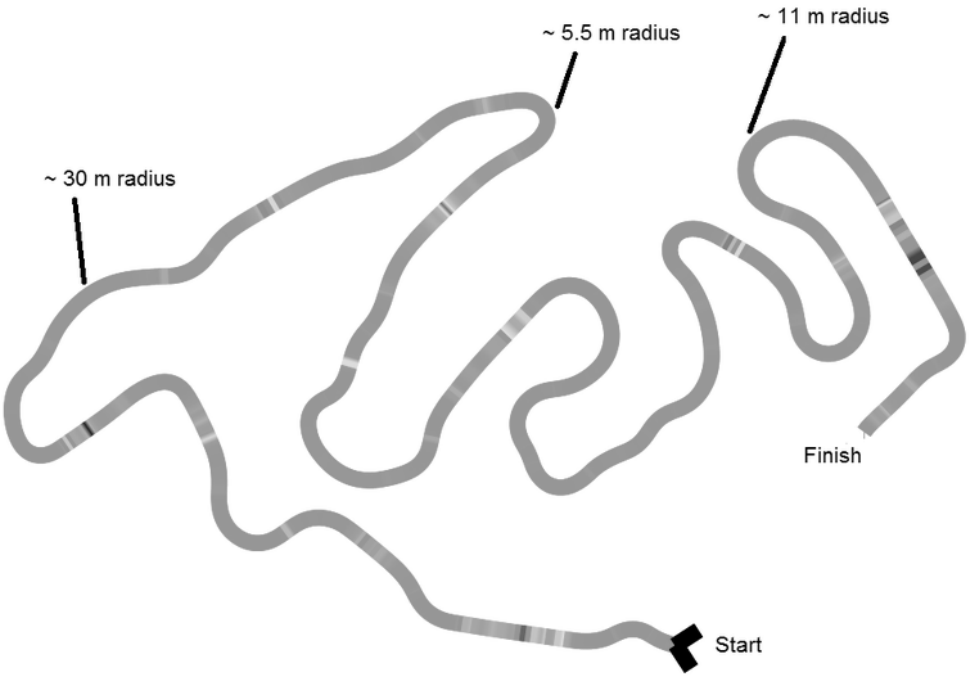

FIGURE 1.2: A typical European Formula Student track. Here the outline of the 2012 Formula Student sprint competition track at Hockenheimring in Germany is given. A few corner radii are indicated. Note that the radius of the corners are quite low compared to the vehicle total lengths of about 2.8 m.

such a case, hardly any yaw angle can be considered very large in comparison. Further, vehicle slip angles are commonly only up to 15 degrees. This raises the question; what happens to the aerodynamic performance of and the vehicle handling characteristics of the car?

Some previous work has been concerned with the case modelling flow around a turning car. Watanabe and Matsuno [5] presented a computational modelling approach of a car going through a hairpin turn using a moving computational grid for the vehicle. As expected, the model showed a shift in the vehicles pressure distribution and predicted a side force generated by the relative difference in the air velocity over the width of the car. Another CFD study by Keogh et.al. [6] investigated the effects of cornering on an inverted wing with end-plates in ground effect. The study used reference frame motion to create a rotating flow relative to the wing. It was found that for the wing and corner index in question (0.01) only a small impact on the overall generation of lift was produced, relative to the straight line motion. However, the study concluded that a significant impact may be found on race cars capable of following paths of larger degrees of curvature through a corner.

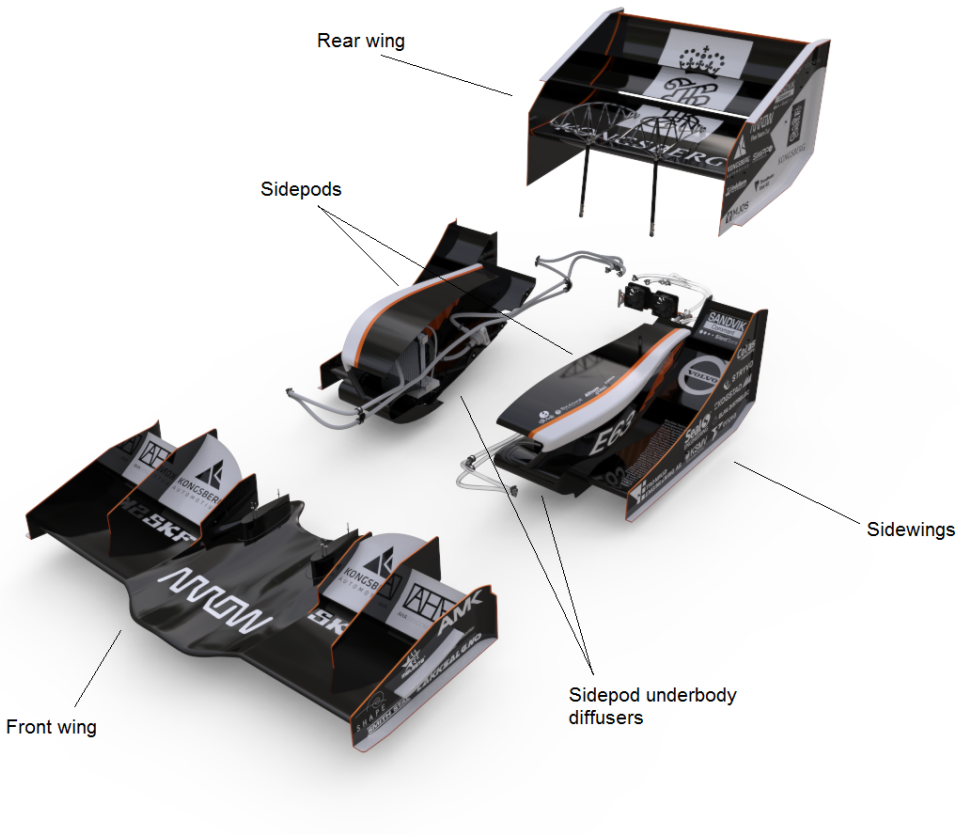

FIGURE 1.3: The aerodynamic lift generating devices implemented in the 2016 Revolve NTNU car. The more traditional front and rear wings are accompanied with large side under body diffusers, as well as 3-element side wings in ground effect. Also shown are the side-pods, used to capture and guide air trough the engine radiators. Render courtesy of Revolve NTNU.

1.3 CFD as an analysis tool, verification and validation and the StarCCM+ software package

Due to the relative complexity of setting up rigid body experiments for a race-car in corners [6], a Computational Fluid Dynamics approach was chosen to study the problem at hand. CFD solvers is also the main tool used by Revolve NTNU for designing the aerodynamic devices implemented on the race-cars, and a further investigation of the accuracy of the models was deemed valuable.

Numerical simulations of fluid flow problems promises a relatively cheap and fast way of assessing key characteristics of engineering problems, compared to wind tunnel tests. However, they are of little value without experimental reference data. This study follows the process of verification and validation outlined in Versteeg [7], heavily influenced by Roache [8], and aims to assess the aerodynamic performance of the race-car Gnist, as well as investigate aerodynamic effects while cornering. The study focuses on steady state Reynolds Averaged Navier Stokes simulations, using one and two equation turbulence

models. While many CFD packages exists, the work was conducted with the software suite StarCCM+ developed by CD-Adapco. The software comes with is's own integrated CAD solution, as well as numerical grid generators, and supports a range of numerical solvers and closure schemes.

Chapter 2

Background

This chapter is meant to give some brief relevant background information on race-car aerodynamics and vehicle dynamics, as well as the CFD modelling in question. The reader is assumed to have some background knowledge in aerodynamics[1].

2.1 Race-car aerodynamics and vehicle dynamics

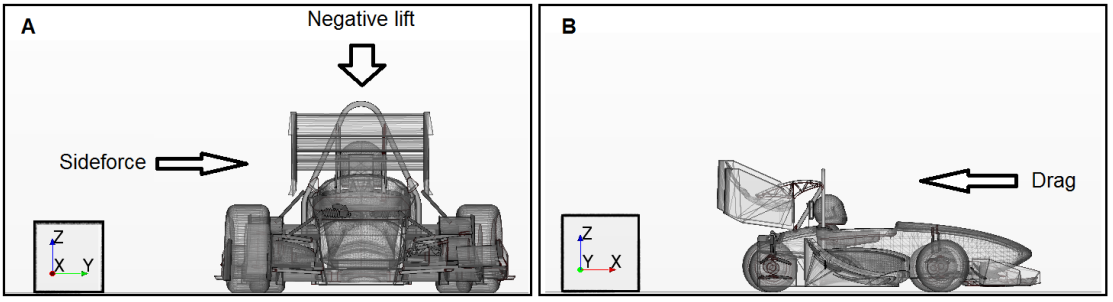

FIGURE 2.1: Aerodynamic forces on a car decomposed into directions along x,y and z. The origin of the coordinate system aligns with the mid-point between the rear and front axles. In A: The frontal view of the car, where the shaded area represents the frontal reference area A_{ref}. In B: Side view of the car.

2.1.1 Race-car performance enhancement through aerodynamic devices

For any conventional car, all steering and driving forces acts through the tire contact patches with the ground as presented in figure 2.1. When the tangential forces exerted on these contact patches exceeds a certain limit, the tires will begin to slide, and the

[1]For an in depth discussion on vehicle dynamics, see for example Pacejka [9] or Milliken and Milliken [10]. For an in depth discussion on race-car aerodynamics, see for example Katz [4].

vehicle becomes increasingly hard to handle. In general, forces absorbed by a tire will result in a deformation, which again will lead to tire *slip* [9]. Although a function of slip, and deformation, a tire's adhesive force, or grip is dependent on the normal force F_z, as well as the friction coefficient μ_f between the tire and track surface. For small values of slip there exists a linear relationship so that

$$F_i = \mu_{f_i} F_z, \qquad i = x, y. \tag{2.1}$$

Also, we may for a given tire contact patch define a non constant maximum adhesion coefficient μ_{peak} such that the maximum available grip can be described as

$$F_{grip} = g \sum F_i = g(\mu_{f_x} + \mu_{f_y}) F_z = \mu_{peak} F_z f. \tag{2.2}$$

Here g and f are some functions of the tires state, whose values are not greater than 1[2]. The same argument can be generalized for the whole vehicle and qualitatively we may visualize the sum of available grip with the model sometimes referred to as the *friction coefficient circle* [4], given in figure 2.2.[3]

If we look at the vehicle as a point, of mass m, driving along a circular path with radius r in the xy-plane, we have the *maximum* tangential velocity, v_{max}, as a function of grip only;

$$v_{max} = \sqrt{\frac{\tilde{F_{grip}} r}{m}} = \sqrt{\frac{\tilde{\mu_{peak}} \tilde{F}_z \tilde{f} r}{m}} = \sqrt{\frac{\tilde{\mu_{peak}} (gm + DF) \tilde{f} r}{m}}. \tag{2.3}$$

In equation 2.3, g is the gravitational acceleration, DF is the negative aerodynamic lift, or down-force, of the car defined as positive along -z in the coordinate system introduced in 2.1 and tilde marks properties now related to the car, rather than a single tire. In general, DF is itself a function of both velocity and mass, as the weight of the aerodynamic package is a design variable. From this it is clear that one can only hope to gain an increase in maximum cornering speed if one manages to increase F_z by a factor more than proportional to an in increase in m. Further, the maximum grip is again a function of the vehicle's state $\tilde{f}$[4]. In this study the concern is of the vehicle's state as a

[2] One such function, perhaps familiar to the vehicle dynamics engineer, is the semi-empirical formula named the *Magic formula*, by Pacejka [9]

[3] Because aerodynamic forces can increase normal loads on tires, and thereby grip, aerodynamic performance is not just about racing then, but also about safety. Increasing the normal forces on a road car would mean that in everyday conditions it's grip limit would be increased, creating a larger potential barrier between a driver and an accident or improving performance characteristics in the face of one.

[4] Strictly speaking, μ_{peak} may also be a function of F_z itself [9]

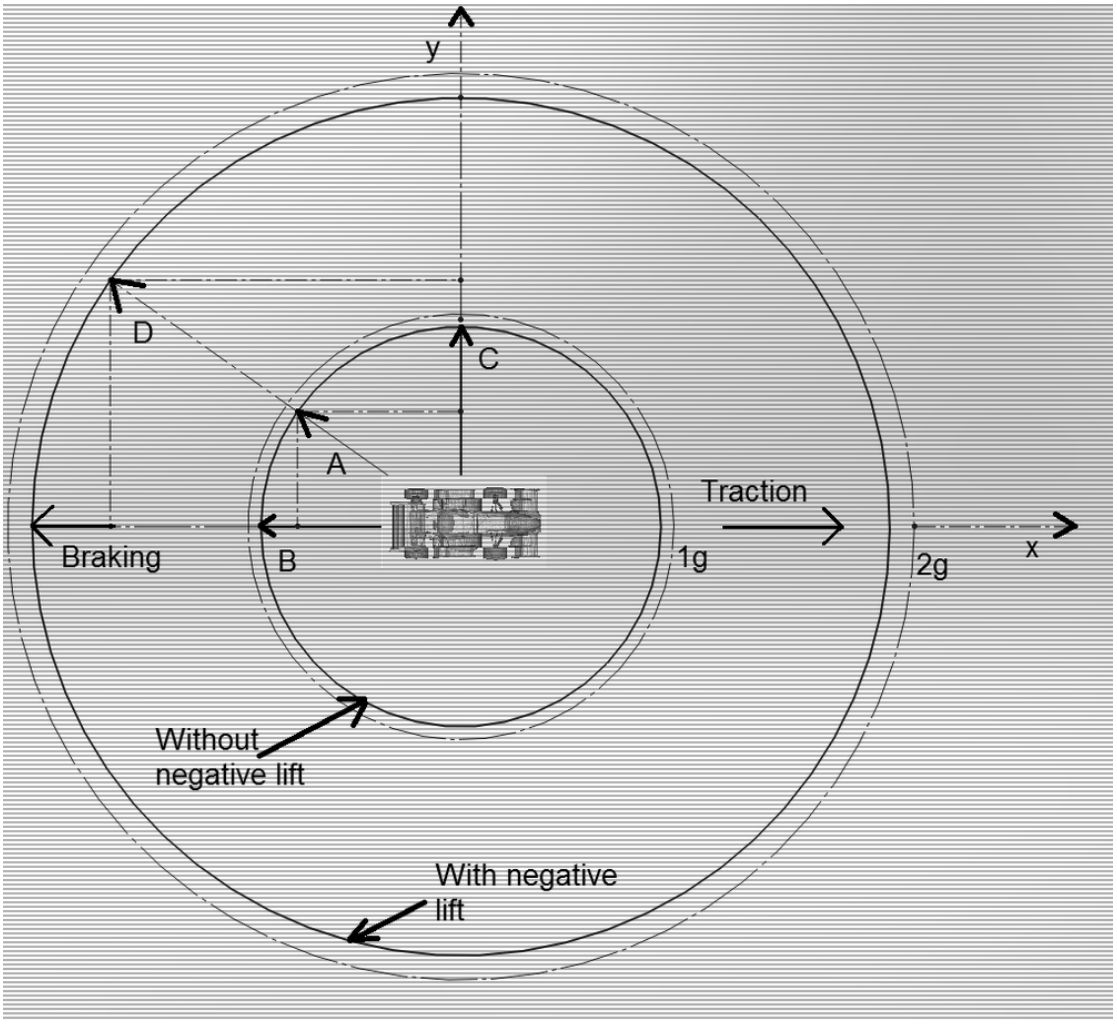

FIGURE 2.2: An illustration of the circle of grip, in terms of vehicle maximum acceleration capacity. Here the vehicle is driving along x. Radial units in terms of the gravitational acceleration g.

function of the airflow predicted in corners by CFD modelling. By the vehicle's state is meant the moments induced by aerodynamic forces about the vehicle's yaw, pitch and roll axes, as presented in figure 2.4, as well as overall lift, drag and side forces.

2.1.2 Vehicle dynamics and the cornering condition

Vehicle slip angle necessary to turn for a front steer car [4], illustrated in figure 2.3, can be defined as the angle between the direction that a vehicle is heading, and the direction of it's instantaneous velocity. This angle will then be responsible for a yaw angle, the angle with which air hits the car, with respect to it's longitudinal center line. In general, a yaw angle can be introduced by both side winds and gusts, but for the present study it is assumed that the free stream velocity of the air with respect to the car, is only

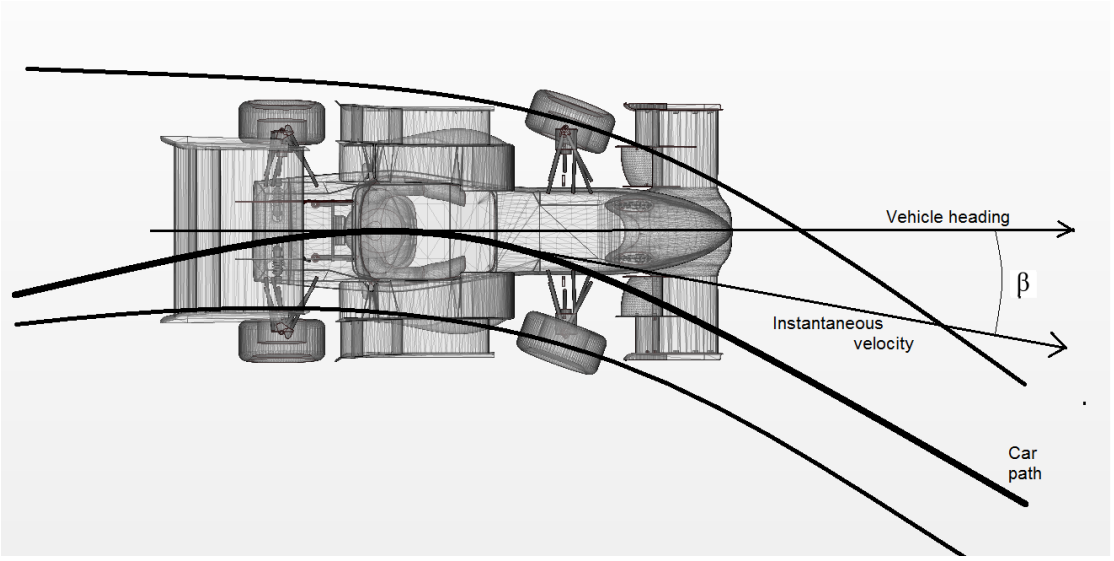

FIGURE 2.3: Car slip angle. The angle between the car longitudinal axis, and the direction of the instantaneous velocity.

induced by the vehicles' velocity itself, so that the yaw angle is equal to the vehicle slip angle.

In an open road case turn, a vehicle follows a curved path through the air. As it does, weight transfer generally leads to a roll angle about the axis illustrated in figure 2.4. For a conventional car, having a centre of gravity above the height of the roll axis, this leads to the car leaning out of the turn. In race cars that utilize ground effect aerodynamic devices, as explained in the next section, this means that the asymmetry of the alignment of the car with respect to a horizontally aligned ground can create a significant moment about the roll axis. Depending on where along the ground effect curve the car as a whole is located, this roll can even create a self re-enforcing effect. The same holds for a car braking, creating a positive pitch angle from weight transfer. In this study, a steady state cornering vehicle is investigated, so that it's pitch is assumed to be zero. Then we are left with roll and yaw angles.

2.1.3 Ground effect

In race-car aerodynamics, one effect that makes a profound difference in a vehicles handling is the ground effect. The ground effect refers to a wing's relatively rapid increase in lift as a function of it's decreasing height over the ground [4]. For an inverted wing, such as on a race car front wing, the effect is sometimes partially explained through the venturi effect, augmenting the low pressure generation on the suction side of the wing. However, ground effects has also been shown to be important to aircraft wing performance near ground [11]. For race-cars the topic is, and has been for the last 30

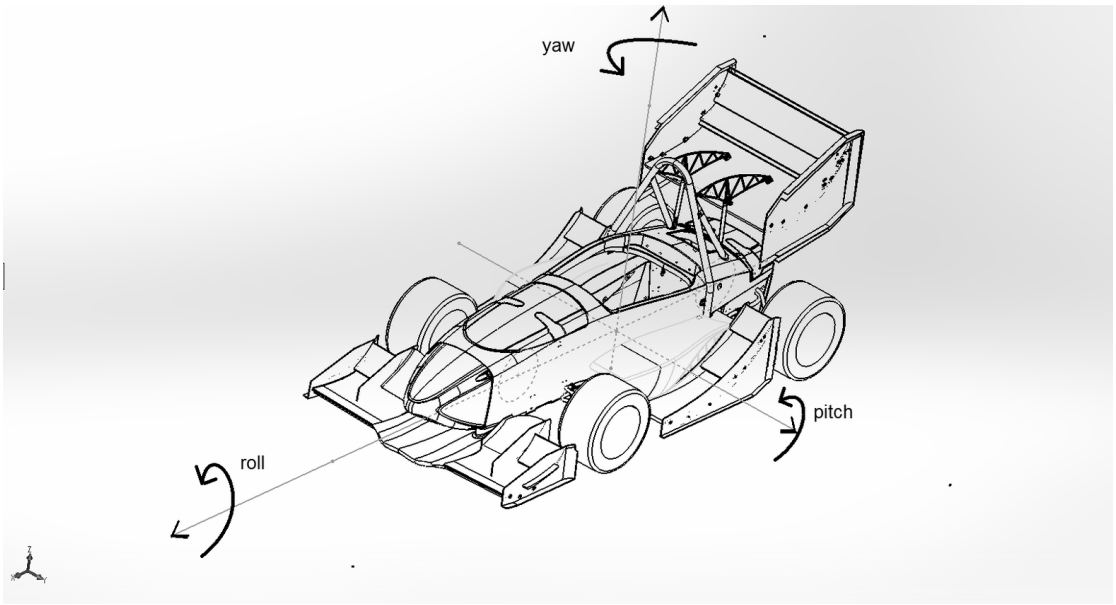

FIGURE 2.4: The three axes of rotation defining the yaw, roll and pitch angles. Positive rotation as defined by the right hand rule. All angles are defined with respect to a vehicle running in a straight line.

or so years, subject to a substantial amount of research [12], and the typical result for a generic wing in ground effect with end plates is illustrated in figure 2.5.

2.1.4 Air compressibility effects

The ground effect utilized in race car aerodynamic design leads to often highly accelerated air flows underneath wings and tires, which again can lead to air being compressed even at relatively low free flow mach numbers. A recent study by Keogh [13] was concerned with compressibility effects predicted by RANS turbulence modelling of air moving around a open wheel race car utilizing aerodynamic devices in ground effect. The study concluded that significant compressibility effects were seen for free stream mach numbers as low as 0.0882. Here the largest deviations from the incompressible ideal case were generated around the vehicle under body diffusers and tires, where differences of more than 1 percent where observed. Another study by Doig [13] investigated compressibility effects around a single inverted airfoil as predicted by RANS simulations, and compared with incompressible simulations as well as experimental data. The study found significant deviations in lift and drag prediction for the wing at mach numbers as low as 0.15, equating to a Reynolds number, Re, of around 780 thousand. The height to chord ratio's investigated were between 0.067 and 0.313. These conditions are close to the flow conditions simulated in this study, as will be presented later, and one can assume that compressibility effects may be significant.

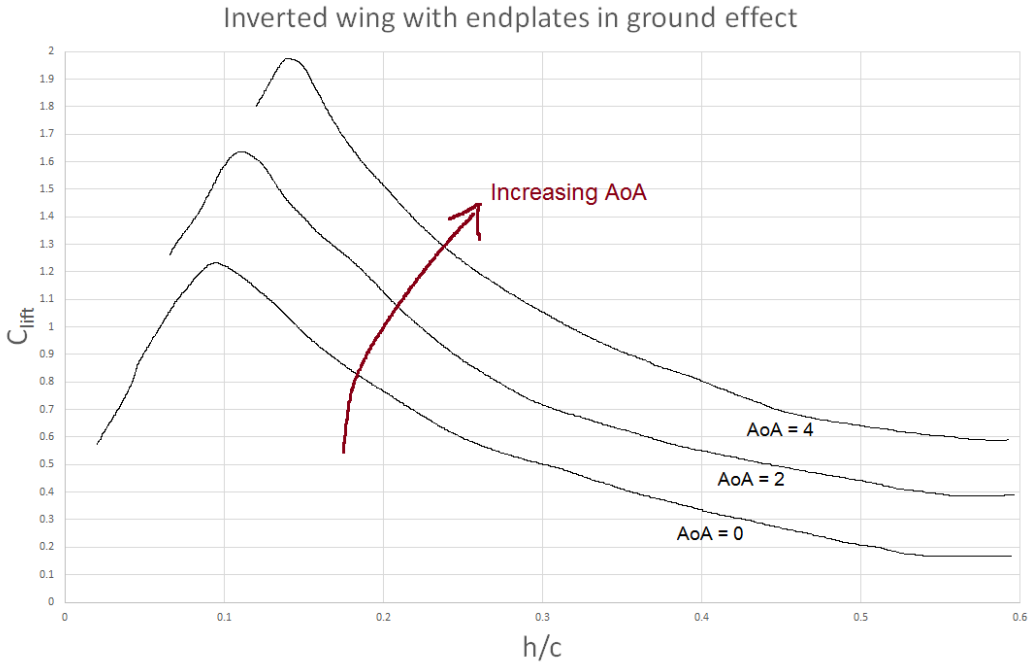

FIGURE 2.5: The typical relation between a generic inverted wings' lift coefficient and its height above ground to chord length ratio, h/c. For increasing angles of attack, AoA, the lift peak is shifted towards larger values, and becomes more narrow.

2.2 CFD simulations and governing equations

2.2.1 Steady state RANS and turbulence modelling

Turbulence is an inherently unsteady, random, three dimensional phenomena, which requires a very high level of grid refinement and large computational power in order to solve for, such as in a Direct Numerical Simulation (DNS). Reynolds-averaged Navier Stokes (RANS) simulation turbulence models attempt to bypass these requirements by modelling turbulence through the use of a varying number of auxiliary (in the non mathematical general sense) equations and transport equations. This work focuses on steady state RANS simulations using one (Spalart-Allmaras)- or two ($k-\varepsilon$ & $k-\omega$)-equation turbulence models. Only a very brief introduction of these are given here. For an introduction to CFD in general see for example Versteg & Malalasekera [7] or Ferziger & Peric [14].

Versteeg & Malalasekera cites without proof from Anderson et. al [15] the following formulation of the RANS equations for turbulent compressible flows:

$$\frac{\partial \bar{\rho}}{\partial t} + \mathrm{div}(\bar{\rho}\tilde{\mathbf{U}}) = 0 \tag{2.4}$$

$$\frac{\partial(\bar{\rho}\tilde{U})}{\partial t}+\text{div}(\bar{\rho}\tilde{U}\tilde{\mathbf{U}}) = -\frac{\partial \bar{P}}{\partial x}+\text{div}(\mu \text{ grad } \tilde{U})+\left\{-\frac{\partial(\overline{\bar{\rho}u'^2})}{\partial x}-\frac{\partial(\overline{\bar{\rho}u'v'})}{\partial y}-\frac{\partial(\overline{\bar{\rho}u'w'})}{\partial z}\right\}+S_{M_x} \tag{2.5}$$

$$\frac{\partial(\bar{\rho}\tilde{V})}{\partial t}+\text{div}(\bar{\rho}\tilde{V}\tilde{\mathbf{U}}) = -\frac{\partial \bar{P}}{\partial y}+\text{div}(\mu \text{ grad } \tilde{V})+\left\{-\frac{\partial(\overline{\bar{\rho}u'v'})}{\partial x}-\frac{\partial(\overline{\bar{\rho}v'^2})}{\partial y}-\frac{\partial(\overline{\bar{\rho}v'w'})}{\partial z}\right\}+S_{M_y} \tag{2.6}$$

$$\frac{\partial(\bar{\rho}\tilde{W})}{\partial t}+\text{div}(\bar{\rho}\tilde{W}\tilde{\mathbf{U}}) = -\frac{\partial \bar{P}}{\partial z}+\text{div}(\mu \text{ grad } \tilde{W})+\left\{-\frac{\partial(\overline{\bar{\rho}u'w'})}{\partial x}-\frac{\partial(\overline{\bar{\rho}v'w'})}{\partial y}-\frac{\partial(\overline{\bar{\rho}w'^2})}{\partial z}\right\}+S_{M_z} \tag{2.7}$$

$$\frac{\partial(\bar{\rho}\tilde{\Phi})}{\partial t}+\text{div}(\bar{\rho}\tilde{\Phi}\tilde{\mathbf{U}}) = \text{div}(\Gamma_\Phi \text{ grad } \tilde{\Phi})+\left\{-\frac{\partial(\overline{\bar{\rho}u'\phi'})}{\partial x}-\frac{\partial(\overline{\bar{\rho}v'\phi'})}{\partial y}-\frac{\partial(\overline{\bar{\rho}w'\phi'})}{\partial z}\right\}+S_\Phi \tag{2.8}$$

Central to the formulation of these equations, is the concept of representing turbulent flow variables through *Reynolds decomposition*, that is, as random fluctuations around a mean value. The notation adopted is that upper case letters (U, V, W, Φ, P) represent mean flow variables, while lower case primed letters (u', v', w', ϕ') represent the fluctuating parts of their respective upper case versions, with the density ρ an exception. Further, the tilde represents density weighted variables. Here then, equation 2.4 represents the familiar continuity relation, but with respect to the density weighted mean flow velocity vector $\tilde{\mathbf{U}}$ and the time-averaged density $\bar{\rho}$. Equation 2.5- 2.7 are the so-called *Reynolds equations*, with mean flow velocity components $\tilde{U}, \tilde{V}, \tilde{W}$, time averaged pressure $\bar{P}$, viscosity μ , and momentum source terms $S_{M_x}, S_{M_y}, S_{M_z}$, which also contains contribution from the viscous stresses connected with the second viscosity, otherwise known as the bulk viscosity [16]. Equation 2.8 represents a scalar transport equation of some scalar density weighted mean variable $\tilde{\Phi}$, with a diffusion coefficient Γ_Φ, source term S_Φ and fluctuating component ϕ'.

The task of the RANS turbulence models is to predict values for the six independent terms in 2.5- 2.7; $\overline{\bar{\rho}u'^2}$, $\overline{\bar{\rho}u'v'}$, $\overline{\bar{\rho}u'w'}$, $\overline{\bar{\rho}v'^2}$, $\overline{\bar{\rho}v'w'}$ and $\overline{\bar{\rho}w'^2}$, dubbed the *Reynolds stresses*, as well as the averaged fluctuating terms in the scalar transport equation; $\overline{\bar{\rho}u'\phi'}$, $\overline{\bar{\rho}v'\phi'}$, $\overline{\bar{\rho}w'\phi'}$, rather than having to solve for all of them. The Spalart-Allmaras [17] turbulence model uses one transport equation, hence is dubbed a one-equation turbulence model.

Conveniently forgetting about compressibility for a moment, the model solves for a kinematic eddy viscosity parameter $\tilde{\nu}$, and relates it to the Reynolds stresses through the relation;

$$-\rho\overline{u_i' u_j'} = 2\mu_t S_{ij} = \rho\tilde{\nu} f_{\nu 1}\left\{\frac{\partial U_i}{\partial x_j} + \frac{\partial U_j}{\partial x_i}\right\} \tag{2.9}$$

in tensor notation. Here μ_t is the eddy, or turbulent viscosity. This is related to the model's viscosity parameter through a wall damping function $f_{\nu 1}$, specific to the model. Reportedly, the relation given in eq. 2.10 is the same for both the compressible and the incompressible versions of the model, but their transport equations differ slightly [18, 19] and its formulation is omitted.

Both two-equation turbulence models used here, the Realizable $k-\varepsilon$ model [20] and the Menter (SST) $k-\omega$ model [21], predicts Reynolds stresses by assuming the Boussinesq approximation,

$$-\rho\overline{u_i' u_j'} = \mu_t\left\{\frac{\partial U_i}{\partial x_j} + \frac{\partial U_j}{\partial x_i}\right\} - \frac{2}{3}\rho k\delta_{ij} \tag{2.10}$$

as well as solving their respective pairs of transport equations. In the above relation, $k = \frac{1}{2}(\overline{u'^2} + \overline{v'^2} + \overline{w'^2})$, is the turbulent kinetic energy central to both models, and δ_{ij} is the Kronecker delta.

The classic turbulence model versions have been continuously developed and assessed since their time of creation, and a further outline of the models' transport equations are, again, omitted. All of the above mentioned turbulence models come with their own (substantial) set of auxiliary equations as well as empirically derived transport equation coefficients, which may even differ slightly in different CFD packages[5].

2.2.2 Wall treatment and y+ values

The low wall y^+ treatment makes no explicit modelling assumptions, and sets the the velocity distribution in the viscous sublayer as $u^+_{laminar} = y^+$. The velocity distribution in the logarithmic layer is set to

$$u^+_{turbulent} = \frac{1}{\kappa} ln(Ey^+) \tag{2.11}$$

[5]Star-CCM+ v.10.02 however, was found to use largely the same model coefficients as those defined in OpenFOAM v.2.4.0 by default.

, where the von Karman constant $\kappa = 0.42$, and the constant $E = 0.9$, by default. The definition of the dimensionless u^+ and y^+ stems from the usual *law of the wall*, stating that

$$u^+ = \frac{U}{u_t} = f\left(\frac{\rho u_t y}{\mu}\right) = f(y^+) \tag{2.12}$$

, where U is the mean flow velocity magnitude, u_t is the friction velocity, and y is the wall distance. It says that the mean flow velocity close to a wall does not depend on free stream parameters [7].

2.2.3 Numerical discretization errors

For CFD work, Roache [8] presents, as an estimate for the discretization error E_{f_1} of a target quantity f_1 in the finest of two grid levels, the relation;

$$E_{f_1} = \left\{\frac{f_2 - f_1}{1 - r^{p_{num}}}\right\}. \tag{2.13}$$

Here f_2 represents the target variable in the coarser mesh, p_{num} represents the order of the numerical scheme and r represents the refinement ratio between the two meshes. If the fine mesh has a base cell size of 0.2 units, and the coarse mesh has a base cell size of 0.4 units, the refinement ratio is 2 ($r = h_2/h_1 > 1$, where h is some cell base size).

Further, to put some upper bounds on the discretization error, Roache introduced the grid convergence indicator GCI, such that $(GCI)_U = F_S E_U$, for some target variable U, with a discretization error E_U. In this relation, F_S is a safety factor. Roache's recommendation was a safety factor of 3 for conservativeness.

Chapter 3

Methods

3.1 Different simulation approaches to help understand the cornering condition

Here is a presentation of the overall approaches used to model a car going through a corner. The models are split into straight line cases, looking at pure yaw angle effects, and curved domain cases which additionally introduces rotating flow.

3.1.1 Straight line cases

The complete domain is illustrated in figure 3.1. Three different car attitudes were investigated. An illustration of these is presented in figure 3.2. The straight line case with zero yaw and roll angles served as the reference case. Then, a -5 degree yaw angle was introduced, along with a 15 degree turn angle on the wheels. The third case added

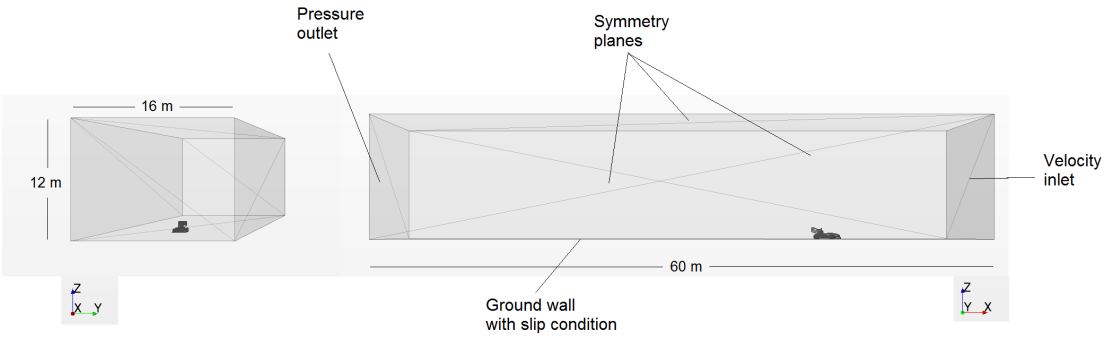

FIGURE 3.1: The dimensions of the computational domain along with definitions of the boundary conditions. Axis orientation of the global reference system is included.

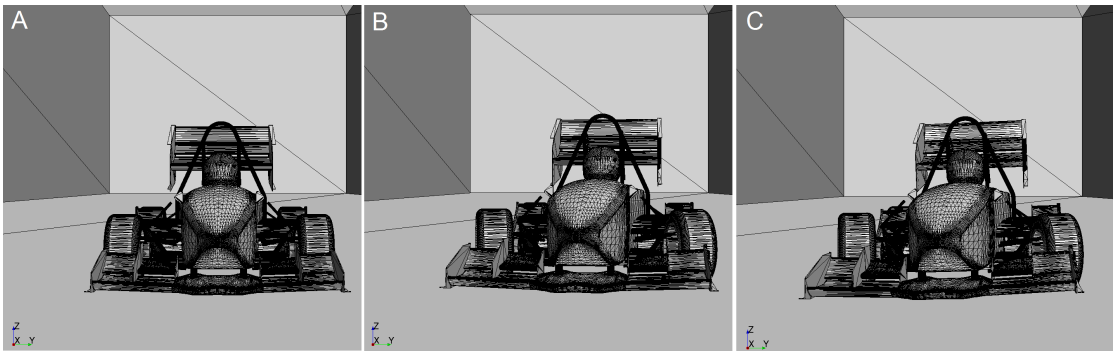

FIGURE 3.2: The three different car geometries used to investigate the affect of yaw vs rotating flow around the car in a turn. In A: the vehicle in the straight ahead configuration; yaw, roll, and pitch equal to zero. In B: The vehicle with a -5 degree yaw angle. In C: Th vehicle with a -5 degree yaw angle, and a 2 degree roll angle.

a 2 degree roll on the -5 degree yaw vehicle[1]. For all cases, the side force, lift and drag-forces were computed with respect to the fixed global reference frame, shown in figure 3.1. Additionally, the momentum about the vehicle's pitch, yaw and roll axis was tracked, to help understand the impact from the differing flows on the vehicle state. The pitch, yaw and roll axes followed the vehicle reference frame, and were separate from the global, fixed reference frame, although for the straight line case with zero yaw and roll, the axes of both reference frames were aligned.

3.1.2 Curved domain cases

In total 4 different curvature radii were investigated, to see the development in the decomposed aerodynamic forces and induced car moments. Figure 3.3 presents the computational domain built for the 14 m radius turn simulations. The remaining domains were built in a similar manner. All the inlet cross sections of the curved domains were equal in size to the straight line domain. The investigated curvature radii were 7, 14, 28, and 56 metres, respectively, measured from the axis of rotation to the centre of the vehicle. Because the goal was to investigate how the flow changes with respect to the car's corner index, the velocity along the curve coinciding with the vehicle centre was kept constant at 16.67 m/s, rounded off to two decimals[2]. This velocity was set by specifying the rotation rate of the rotating reference frame. For each corner radius, the above mentioned vehicle configurations; straight line, yaw and yaw plus roll, were simulated.

[1] These angles were seen to be within reasonable limits, when looking at vehicle log track data from the 2016 competition season.

[2] As such, judging by track log data for the Revolve NTNU 2016 race-car, the 7 m radius turn represents a severe, fictional case with an over performing car in terms of lateral acceleration capability, while the 56 m radius turn represents a severely under performing car with respect to maximum lateral acceleration capability.

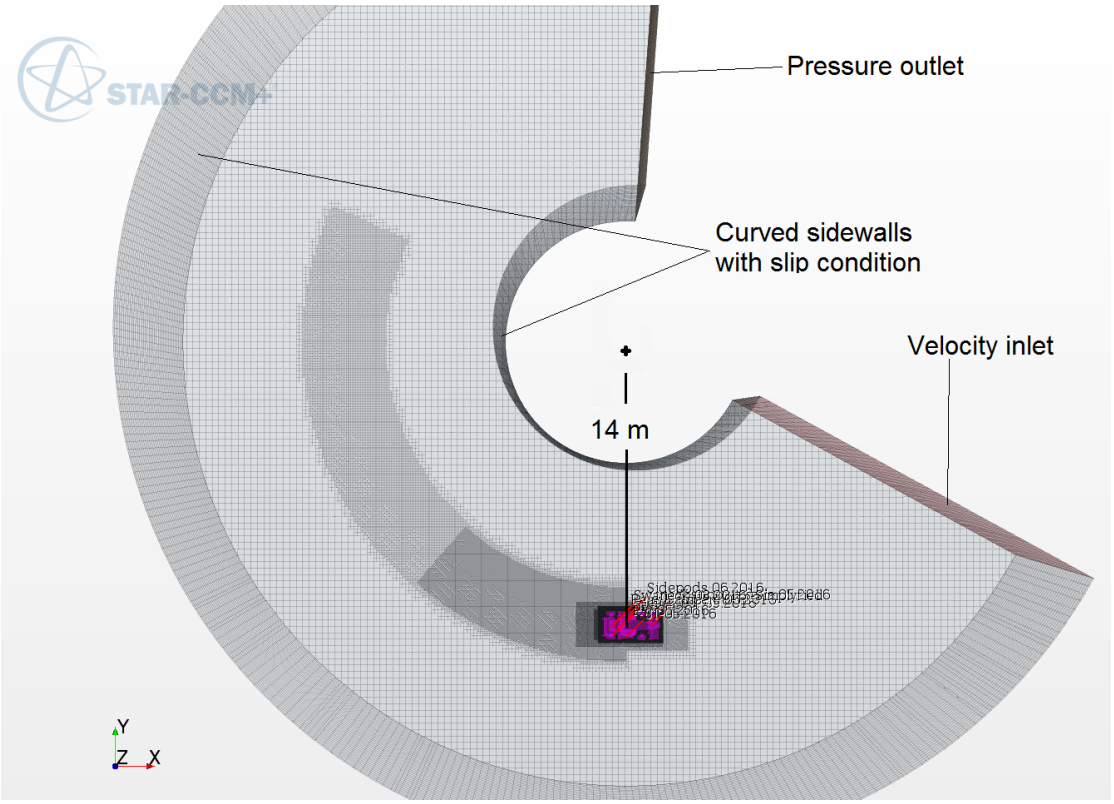

FIGURE 3.3: The curved computational domain for a simulation of a 14 m radius turn. The other turn domains were built in a similar manner. The global reference frame is the same as for the straight tunnel domains, but with an added rotating reference frame with origin at $y = r$. The boundary conditions are also illustrated. The ground and top walls are specified as slip wall and symmetry planes, respectively, just as for the straight tunnel domain.

3.2 Simulation setup

The following presents details about the simulation setup including turbulence models used and the selected solvers. Further, the numerical grids are presented and the selected method of estimating the numerical discretization errors are outlined. Lastly, the selected boundary conditions are given for the different cases, as well as the used wall treatment.

3.2.1 Turbulence models used and physics assumptions

Simulations focused on the Realizable k-ε turbulence model formulation by Shih et. al [20]. Results were checked with the Menter SST k-ω [21] turbulence model as well for the the validation test case, as can be seen in table 4.1 The simplified validation test cases presented in the subsequent section also utilized the Spalart-Allmaras turbulence model [17], in 2D simulations. In a study by Diazinos, Barber and Doig [22], all these models were compared with respect to their ability of reproducing surface pressure distributions

on an isolated race-car tire. Both of the two-equation models gave similar results. Another study by McManus and Zhang [23], investigating similar flows as those produced by open wheels, reported that of the given two-equation models, the Realizable k-ε model proved most accurate in predicting vortex locations and strengths. This, as well as the results in the initial validation cases, made the Realizable k-ε the model of choice for most vehicle simulations.

The modelled medium was set to air in Star-CCM, which automatically sets properties such as dynamic viscosity, and molecular weight. The reference pressure was set to one atmosphere.

All simulations were run using a segregated solver with a second order upwind convection scheme, implemented by a SIMPLE like algorithm [18]. Other modelling assumptions were isothermal flow and compressible, ideal gas, as justified by the previous investigations [13, 24] mentioned in chapter 2.

3.2.2 Numerical grids and discretization error estimates

The grid, or mesh, for the straight tunnel domain can be seen in figure 3.4. The curved domain simulations used a similar mesh build and refinement level, but used curved wake refinement zones as illustrated in figure 3.3. In all cases, structured hexagonal trimmed meshes were used. In designing the grids, the guide by Spalart [25] has been helpful.

For a discretization error estimate, the work followed the methods suggested by Roache [8], as presented in the previous chapter. A F_s of 3 was selected, and a numerical discretization accuracy of second order assumed. Hence, p_{num}= 2. The results of the grid convergence study is presented in table 4.1 in the next chapter.

In the results later presented uncertainty due to iterative convergence, after a flat-lining of residuals[3] was found to be negligible. Simulations usually converged within 2000 iterative steps, and readings at 2500 steps usually found a difference less than 0.5 %.

3.2.3 Boundary conditions

For the computational domains presented in figure 3.1 and figure 3.3 velocity inlets were used, in combination with pressure outlets at reference pressure. For the specific cases of the curved domain simulations, a velocity inlet specifying a 0 m/s value was used, so

[3]By *flat-lining* of residuals, it is here meant a oscillating behaviour of small amplitudes around a fairly distinct and sufficiently low value. An illustration of the typical behaviour of the relative numerical residuals can be found in the appendix.

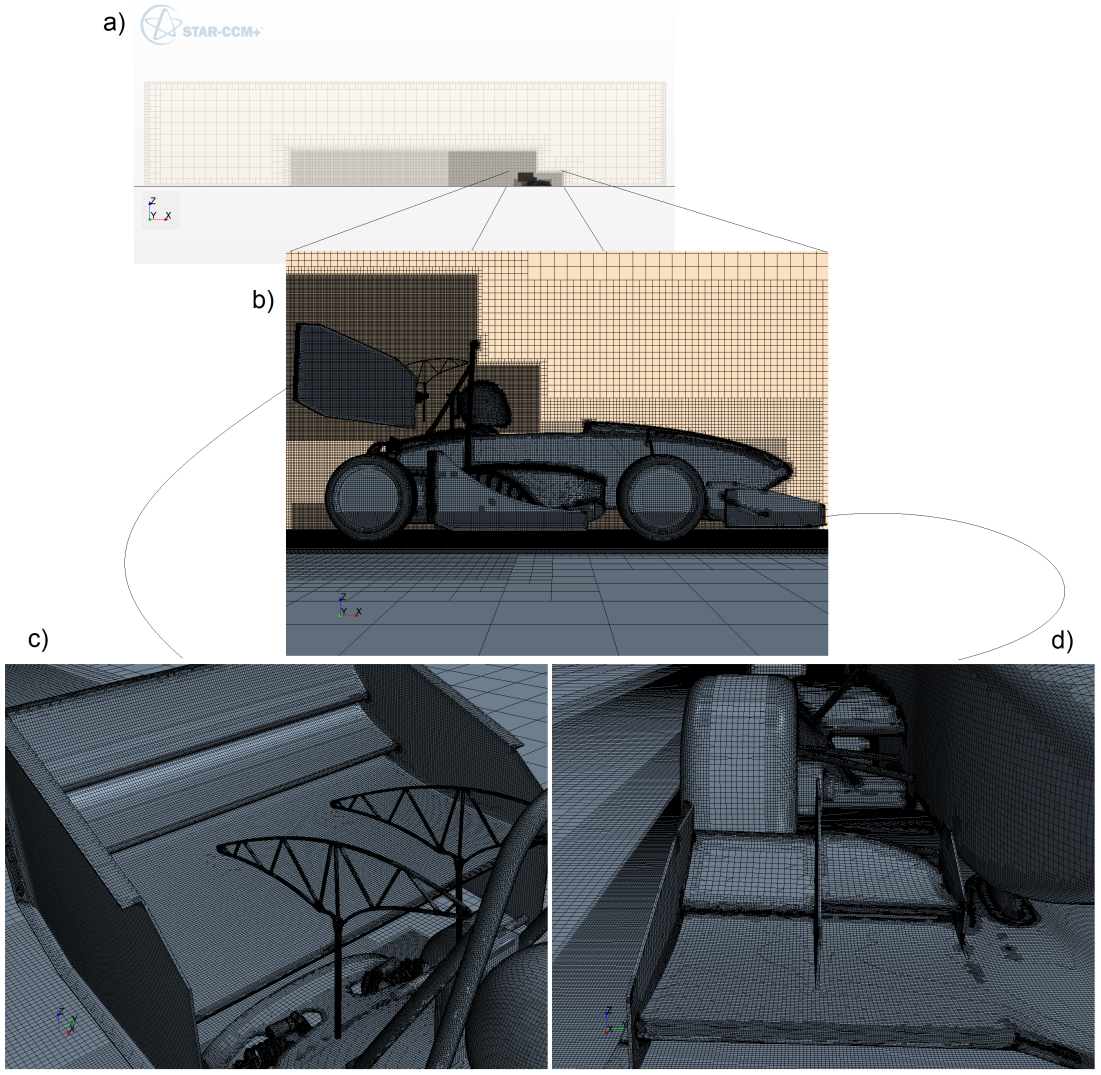

FIGURE 3.4: Illustration of the trimmed mesh used in the simulations. The mesh was built using StarCCM+ surface wrapper, to clean up CAD and give a valid closed surface geometry. In a): An outline of the domain cross section, with the inner and outer wake refinement zones. The outer wake refinement zone stretched more than 10 car lengths downstream of the body. In b): A closer view at the car surface cell distribution and refinement zones along the mid car symmetry plane. In c) a closer view of the rear wing mesh and swan neck. In d): a closer view of the front wing mesh.

that the inlet velocity would only be driven by the rotating reference frame specified for the different curvature radii. StarCCM+ then automatically imposes the motion on the global reference frame through the addition of source terms in the momentum equations, for solving the flow [18]

To simulate an open road case, the boundary specification at the ground surface was set as a wall, but with a non-shear, or slip condition so that there would be no developing

surface boundary layer[4]. For the simulations comparing predicted forces on the car with track test measurements, the wheel surfaces were specified to have tangential velocities matching the free stream velocity, to model tire rotation. In the remaining simulations, for comparing cornering models the tires were fixed, for simplicity.

The block top surfaces of all domains were set to symmetry planes. Symmetry planes were also set for the straight tunnel domain sidewalls. However, in the curved tunnel domains, these sidewalls had to be set as walls with slip condition, like the ground surface.

In Star-CCM+, one may specify turbulence model parameters, by specifying a turbulence intensity, and turbulence length scale. Due to the relative uncertainty in these parameters for an open road case, these were left to their default values of 1 % and 0.01 m, respectively.

3.2.4 Wall treatment

For all simulations, the Star-CCM+ *all* y^+ wall treatment was used. This treatment automatically switches from a *high* y^+ wall treatment to a *low* y^+ wall treatment when the mesh refinement gives a low enough y^+ value, computed on the closest cell to the wall. This treatment is beneficial when performing a mesh dependency test while also varying the surface refinement of the geometry in question. However, this means that the automatic switch in wall treatment might influence the results, and affect the observed order of the numerical scheme p_{obs}, when going from a coarse mesh to a fine mesh.

All the simulations in this project work (excluding the coarser mesh taking part in the mesh dependency study) were shown to have wall y^+ values well below 3. A surface plot of the car y^+ for the mesh used is presented in figure 3.5. This means that for all surface areas, with the exception of local spikes in y^+ due to mesh irregularities, the boundary layer is modeled using a low y^+ treatment.

3.2.5 Car model and simplifications

While a complete assessment of the level of simplification of the car computer model, with respect to the real life tested version is far outside the scope of this thesis, an indication can be helpful. In figure 3.6 a side by side comparison of the model and actual car geometries are presented. In general, the simulation model has been stripped

[4] Another plausible option would be to specify a ground tangential velocity, matching the free stream velocity. This would perhaps pose more of a challenge in the curved domain simulations, where the ground tangential velocity would have to be a function of the specific radius at any point.

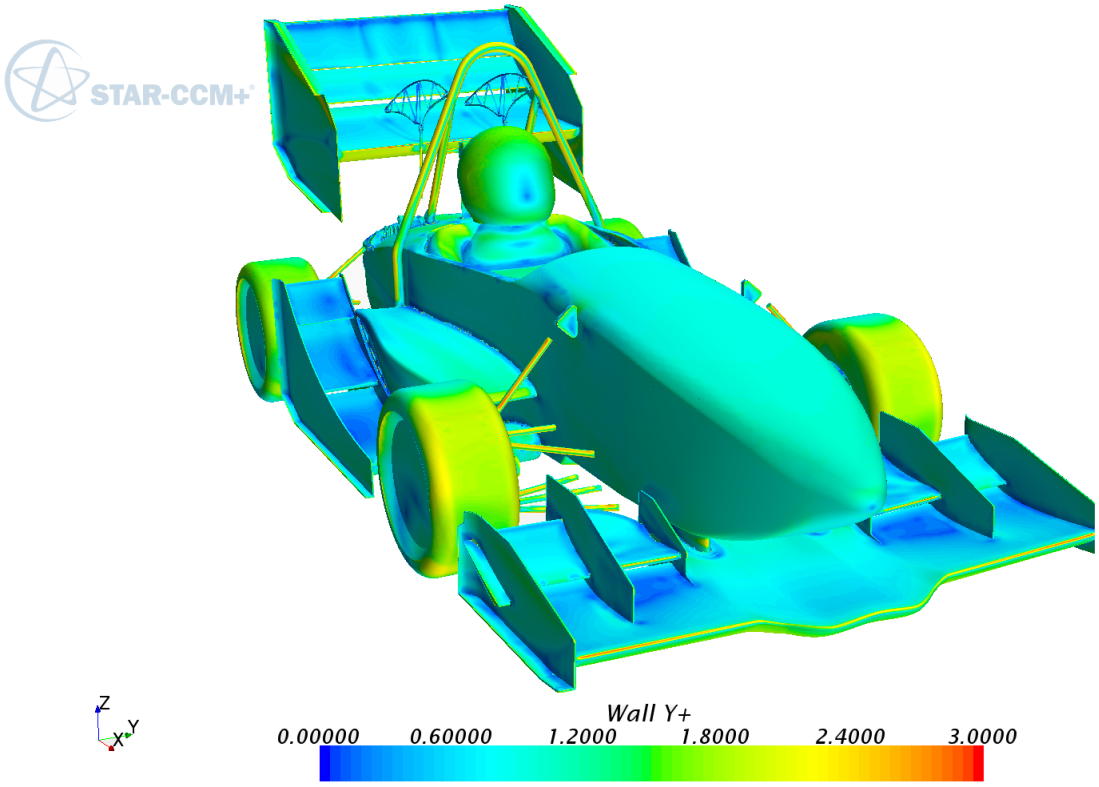

FIGURE 3.5: A surface plot of the wall y^+ on the car. Most values are well below 2.5, but some spikes can be seen on small geometry surfaces and wing leading edges.

of any small geometries deemed not to be too influential to the vehicles overall production of lift. Arguably, some of the additional under body suspension geometry could have been added to the model at relatively low cost, and increased accuracy. We also note discrepancies on the two versions of the main hoop geometry, that might significantly alter the performance of the rear wing. Another, rather large simplification is the lack of a radiator and fan in the model side pods. To completely model these would have been an arduous task, and would have added a relatively large amount of computational cells to the model. Also, only modelling the radiator's as porous regions alone, without the fans to drive the flow, was deemed to be less accurate than simply letting the air flow through freely. In addition, the battery fans drawing air from under the rear damper lid illustrated in figure 3.6, was omitted in the simulation model.

The computer model is of 1:1 scale, and is built using the CAD geometries used to design the moulds of the carbon fibre chassis and wings. As such, tolerance limits for the wing cross sections and chord lengths can be expected to be well within half a millimetre. The relative positioning of the wings with respect to the car chassis, can be expected to have a 2 mm uncertainty. The largest discrepancies occur in wing spans, where a 5 mm error margin in overall lengths is observed when comparing the computer model and the car built. Overall, the AoA of the wings with respect to the car longitudinal axis is

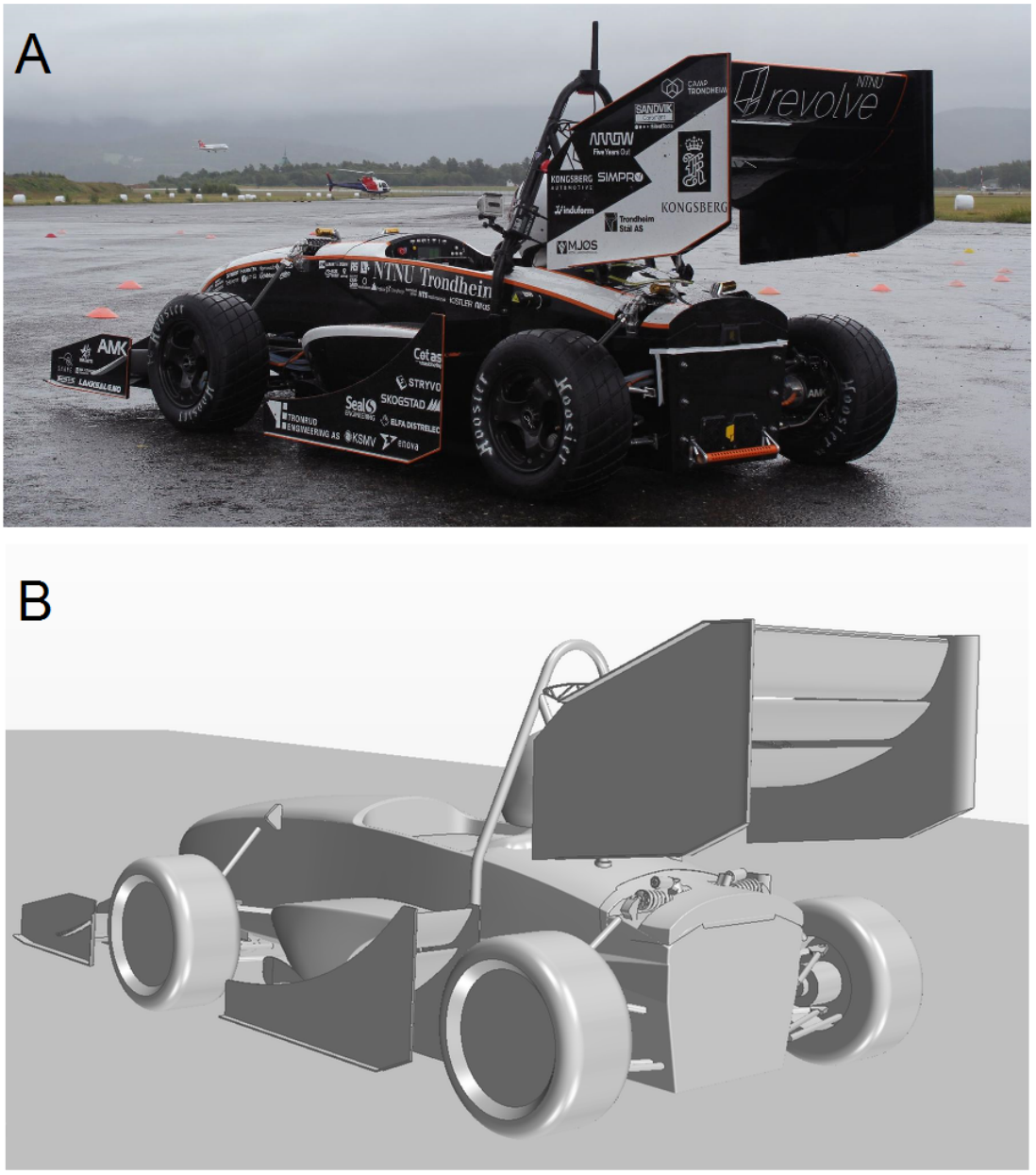

FIGURE 3.6: An illustration to indicate the level of detail omitted in the simplified car model. In A: the car as driven for the validation test case. In B: The 1:1 scale computer model used in the simulations. Note that the rain tires are depicted in A, while the computer model used the dry tire geometries. The wheels rims are closed in the computer model. The computer model is built using the CAD geometries used to mill the carbon fibre moulds for the wings and chassis. As such, the wing cross sections and chord lengths can be expected to be well within half a millimeter tolerance limit.

expected to be within a 1 degree margin. The total length of the vehicle is about 2.9 m, with a total width of about 1.4 m. The frontal reference area was calculated from the computer model generated mesh to be 1.1034 m^2. The actual car is estimated to have a slightly higher frontal reference area, by about 3 %.

Again, this is just to give the reader an idea of the level of simplification, and uncertainty

in the car model geometry. The aim of this study is not to achieve a high fidelity in predicting actual car performance by building a sophisticated model, but to check that the use of the relatively simple RANS approach can give predictions within reasonable limits, and be used to gain an understanding of what happens to a car as it drives through a corner.

3.2.6 Computational system and costs

Simulations were run on NTNU's high performance cluster "Vilje", reserving 5 or 6 computing nodes containing 16 CPU cores running at 2.6 GHz each. The 3D grid generated about 51 million cells, and it took about 4 hours and 30 minutes for the simulations to converge. Post processing was done on a desktop computer with 32Gb installed RAM, and 6 CPU cores running at 3.2 Ghz each.

See table 4.1 for a summary of grid parameters and iteration CPU run times for the Realizable k-ε and the SST $k-\omega$ turbulence models.

3.3 Three validation test cases

Leading up to, and as part of this thesis work, three validation test cases were simulated with varying degrees of geometry complexity. The following presents the different cases studied.

3.3.1 2D and 3D simulations of a single airfoil versus wind tunnel tests

As a part of a project thesis leading up to this work, RANS simulations were conducted on the NREL s826 airfoil, originally designed for use on wind turbine blades [26]. Several measurements on the airfoil had previously been conducted in the wind tunnel at NTNU by Aksnes [27], and this allowed a comparison between experimental and simulated performance data. Both 2D and 3D simulations were run and compared to the wind tunnel measurements. The simulations set up the same case as investigated in the experiments. A figure of the wall to wall wing simulations set up in a computational block section equal in size to the NTNU wind tunnel section can be seen in figure 3.7. The investigation was later further elaborated on, to see if steady state 3D simulations could reproduce such flow effects as stall cells. A complete description of the study and results is given in [28], and is not elaborated here. An excerpt of the results for the wing lift and drag coefficient comparisons are reproduced in the next chapter, for the convenience of the reader.

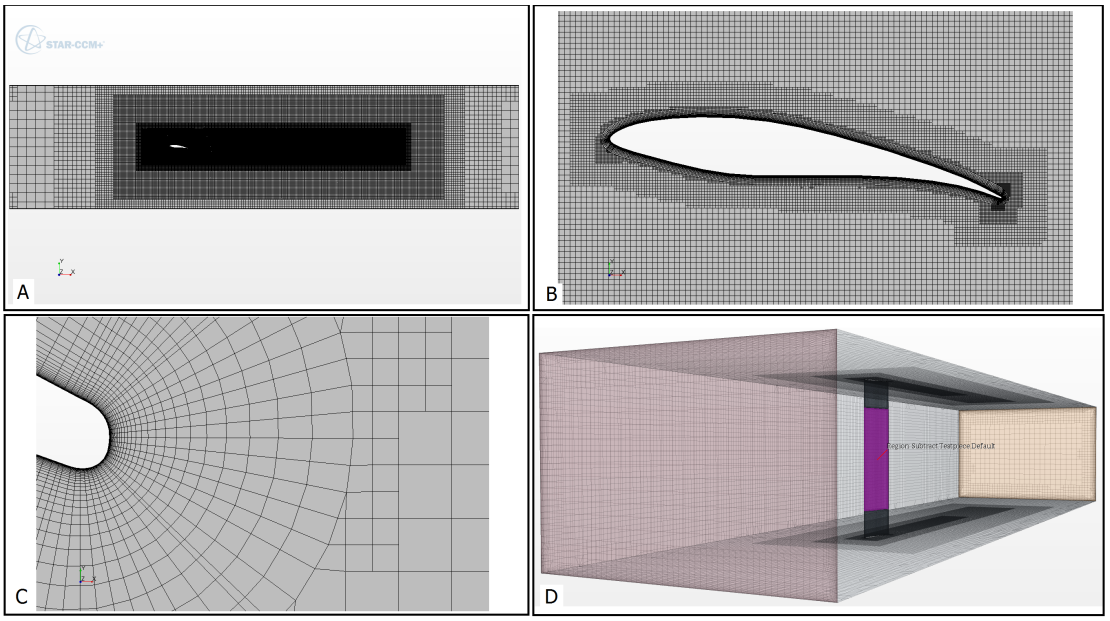

FIGURE 3.7: Numerical grids used for simulations with the NRELs826 airfoil. In A: The mesh used for the 2D simulations. In B: A enlarged view of the wing profile and surrounding grid. In C: An illustration of the 2 mm thick trailing edge and surrounding grid. In D: the 2D mesh extruded into a 3D domain equal in size to the NTNU wind tunnel test section. The measuring section of the wing is highlighted.

3.3.2 Wind tunnel tests of a three element inverted wing versus simulations

To further investigate the ability of the Realizable $k-\varepsilon$ turbulence model to reproduce the flow field around an inverted wing, a wind tunnel experiment using the rear wing of the 2015 Revolve NTNU race car was set up[5]. Simplified test wing end plates was made, making it possible to attach the three element wing configuration to the six-component force balance installed at the NTNU wind tunnel. An illustration of the setup is given in figure 3.8. The exact same setup was then simulated, matching the wing height and tunnel free stream velocities. An illustration of the computational domain and mesh used is given in figure 3.9.

3.3.3 Track test data versus simulations

To get an indication of the DF performance of the car geometry used in this study, Gnist, damper position data from a track test day was analyzed. Gnist utilizes a torque vectoring system that controls the torque given by the 4 individual hub mounted electrical engines to each wheel. This system derives the normal forces exerted on each wheel by measuring the compression on 4 individual car suspension springs, or dampers. This

[5]The initial results of the experiment and simulation comparison was presented as part of the course TEP4545 in engineering fluid mechanics. An elaboration of the study and results is given here.

FIGURE 3.8: The three element wing test piece mounted on the force balance in the NTNU wind tunnel.

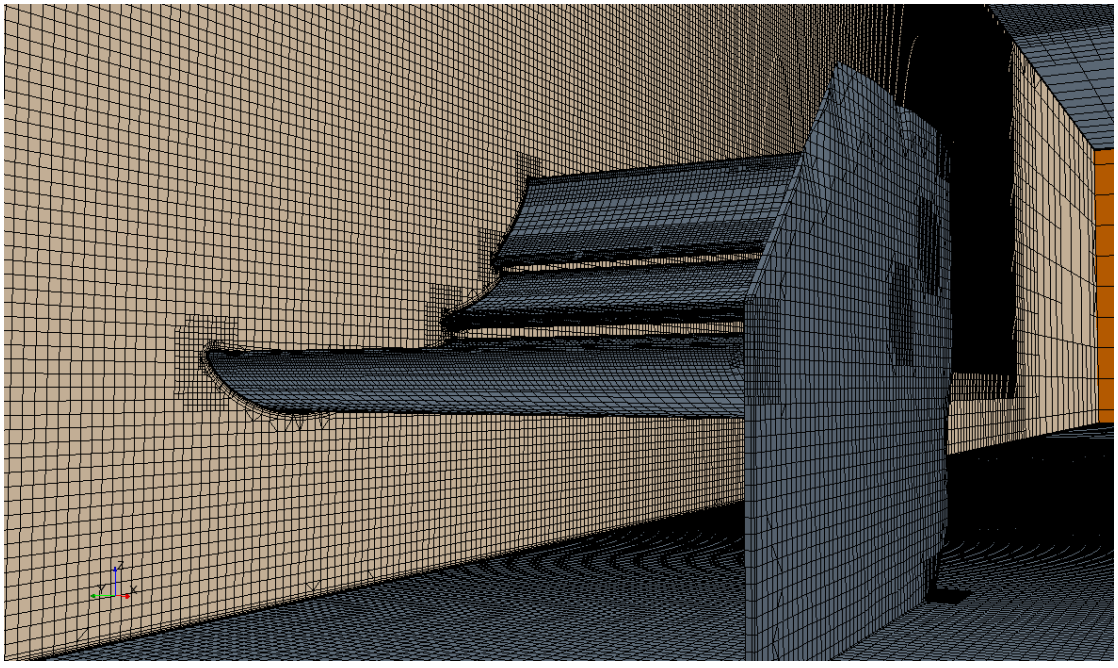

FIGURE 3.9: The mesh used for comparison with the experiment. A high wall y^+ treatment was used.

information is fed from 4 individual damper position sensors, and the normal forces can be calculated via the spring stiffness coefficients and suspension motion ratio. A detailed description of the sensor data acquisition and torque vectoring system on the car can be

found in B. Omholt's master thesis [29].

The car was set to run at a constant speed for roughly 8 second intervals. Data was then sampled from a 5 second interval within the 8 second constant speed intervals, to allow the vehicle to settle, and emulate a steady state driving condition. Car speed was limited by setting the maximum rpm limit of the engines. Because of limited time and resources to conduct the test, a simple method of running the car in opposite directions, and taking the mean of the damper measurements from opposite directions was chosen. Several runs were conducted, to derive a statistical mean and calculate standard deviations of the measured DF. An optical high precision sensor measured the car velocity relative to the ground in both the lateral and longitudinal directions. These velocity measurements were cross checked with an inertial navigation system implemented on the car, and found negligible differences within the sampling times. Measurements were done at Værnes airport, so that the measured local wind speeds by the nearby weather station could be taken into account when analyzing the results. For relatively low wind speeds, the DF measurements obtained from taking the mean of two opposite directions of driving should give a fair indication of the performance of the vehicle at the measured velocity with respect to the ground. The results of the test are given in the next chapter. Naturally, this type of experiment is prone to variation in a wide range of experimental variables, as is indicated by the standard deviations in the measurements from the different runs. All the measurements were however, taken over a total time span of approximately one hour. This is of course not enough to give a meaningful indication of the variation in environmental pressure, density, turbulence intensities and variation in local wind speeds and direction. Hence, the reader is asked to interpret the results accordingly. A further discussion follows in chapter 5.

Chapter 4

Results

Here is presented the range of results from both simulations and measurements. A discussion follows in the next chapter.

4.1 Grid dependency of full car simulations

TABLE 4.1: Grid details. Grid n.2 and n.1 denote the medium and fine meshes, respectively. Presented from left to right then, is the grid type, vehicle drag, vehicle down-force, y^+ maximum value, the total element count in the specific grid (mainly cell count), the relative grid convergence indicator in DF and the standard CPU solver time per iteration.

Grid	D	DF	y^+_{max}	$\#_{tot}$	$GCI_{\%}$	$\triangle_{CPU}$
n.2	237.4	509	2.8	$1.45 \cdot 10^7$	14.7 %	187.6 s
n.1	244.81	527.8	2.5	$5.09 \cdot 10^7$	3.5 %	666.3 s

Table 4.1 presents results from two different grids used for the full car simulations. The $GCI_{\%}$ was computed with respect to the obtained DF values for the vehicle which showed a larger relative discrepancy between grids than D. A safety factor of F_S of 3 was selected, for conservativeness. For these simulations an inlet velocity of 16.67 ms^{-1} was specified. Because the environmental flow variables are the same for both simulations, absolute values are presented. Though computationally much more expensive, the added numerical accuracy of the fine mesh made it the choice for all the subsequent simulations presented here.

4.2 Validation test cases

The following sections present the main results from the three validation tests conducted.

4.2.1 Lift and drag coefficient comparisons for the NRELs826 airfoil

Lift and drag coefficient comparisons for the NRELs826 airfoil are presented in figure 4.1 and 4.2, respectively. For the lift coefficients, NTNU values were obtained both from surface pressure taps located at mid-span, as well as direct force gauge measurements [27], as indicated. DTU experimental values were obtained from direct force balance measurements [30]. For lift, all simulations can be said to give fair estimates. The 2D SST $k-\omega$ turbulence model predicts an onset of stall for a significantly lower AoA, relative to all other simulations.

NTNU experimental drag values was obtained by integrating surface pressure measurements [27]. DTU experimental values was obtained by wake rake measurements, measuring the velocity deficits [30]. Simulation values include both surface skin friction as well as pressure. A fair agreement with the DTU experimental values for drag is observed, especially for the Spalart-Allmaras 2D simulations and the 3D Realizable $k-\varepsilon$ simulations.

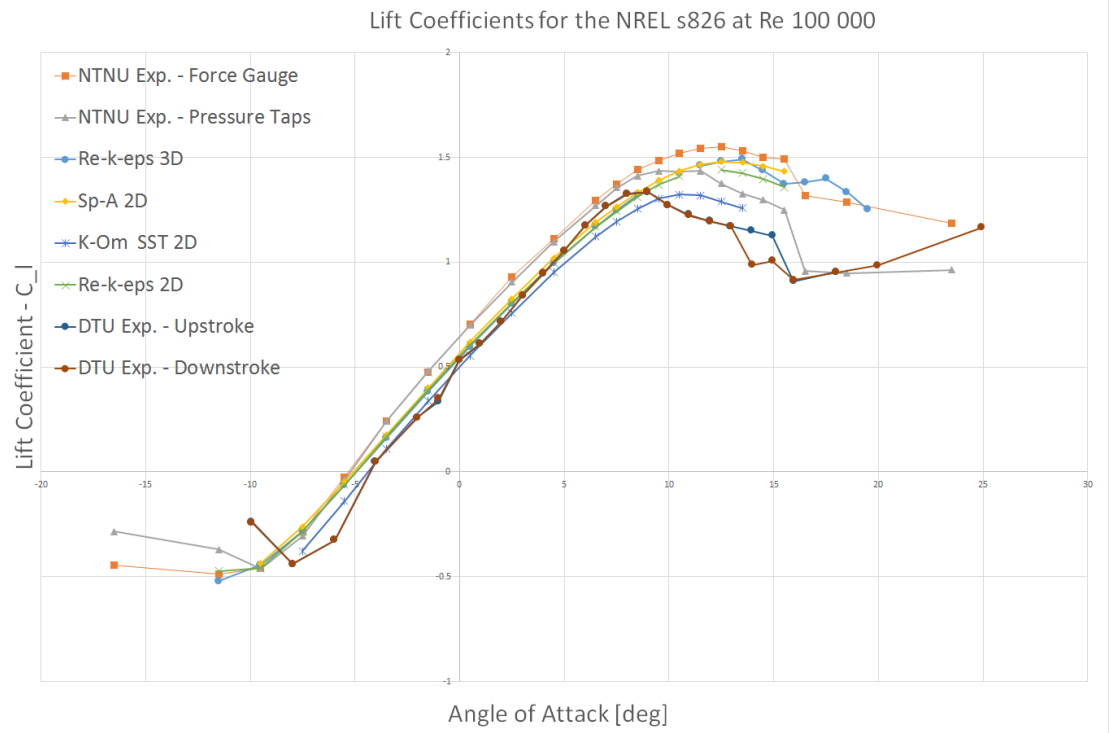

FIGURE 4.1: A comparison of lift coefficients for the airfoil for different angles of attack. Simulations were compared with experimental results from both NTNU and DTU.

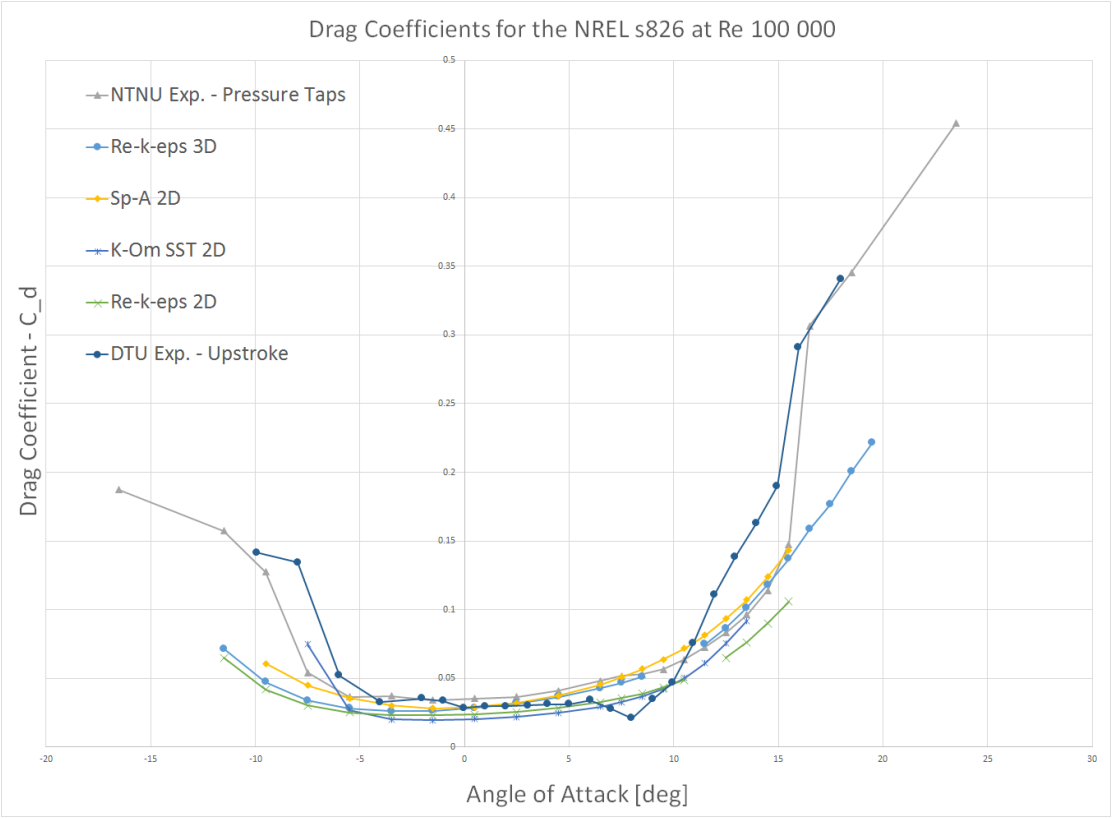

FIGURE 4.2: Simulated and measured drag coefficients for the airfoil at different angles of attack.

4.2.2 Results for the three element inverted wing test case

In figure 4.3 a plot of the measured lift and drag coefficients is given for different free stream velocities. An equal frontal reference area of A_{ref}=0.29 m^2 was assumed for both the simulations and the measurements. Two separate runs with increasing free stream tunnel velocity was conducted in the NTNU wind tunnel. The simulations correlate well with the measurements, falling within the uncertainty of the measurements. Roughly a 5 % discrepancy between the simulations and the first run measurements is observed. A standard deviation in the measurement values was calculated from both run 1 and run 2. The error bands presented with the mean measured forces span two standard deviations relative to the population mean. A plot of measured drag and lift forces for different yaw angles is included in appendix B.

4.2.3 Track test results and full car simulations

In figure 4.4, the results for the vehicle total DF is given, along with predictions from the Realizable $k-\varepsilon$ and SST $k-\omega$ turbulence model simulations. The error bar indicated for the track test measurements span two relative standard deviations, as calculated from

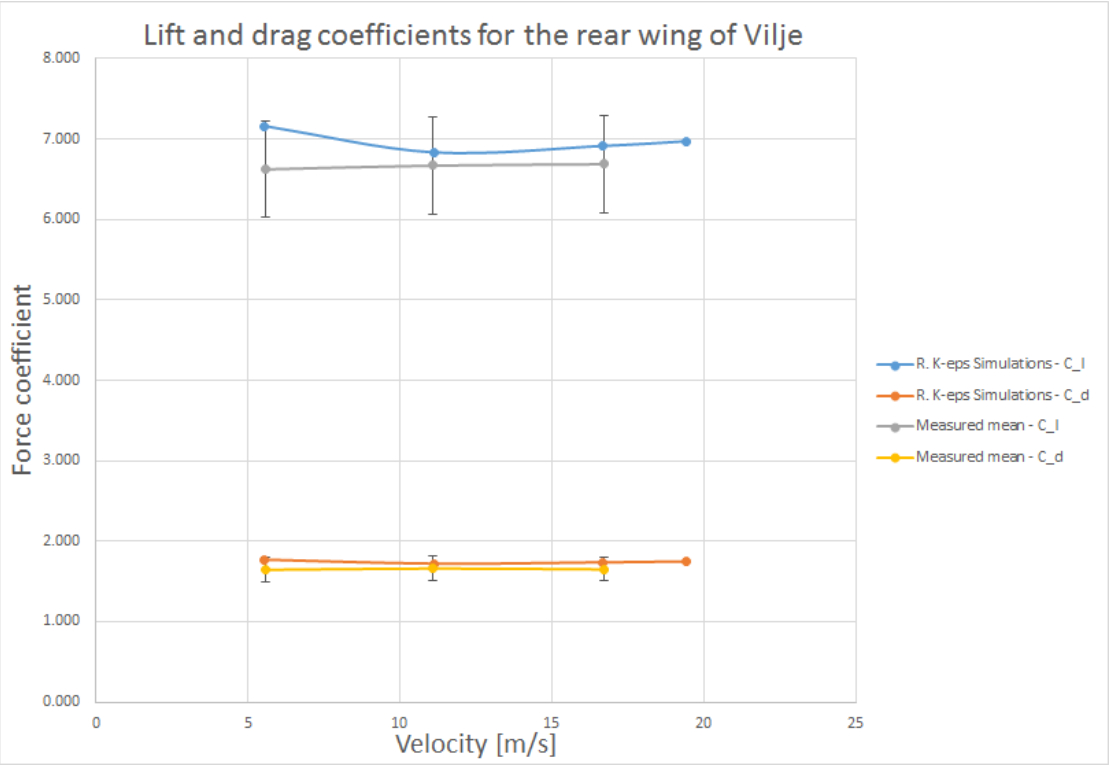

FIGURE 4.3: Measurements vs simulations of the lift and drag coefficients for the 3 element inverted wing at $h/c = 0.44$.

the mean damper displacements recorded for each tire. The simulations are presented with error bars spanning two $GCI_{\%}$. A discussion follows in the next chapter. Figure 4.4 gives a comparison of the velocity fields predicted by the two different turbulence models in the horisontal and vertical planes coinciding with the origin of the reference frame of the car.

4.3 Indirect verification of rotational reference frame domain setup

To indirectly verify that the momentum added from the introduction of the rotational reference frame driving the curved flow in the curved domain vehicle simulations were implemented correctly, the trend of the results for increasing radii was investigated. For large radii the solution should approach the straight line vehicle case, where the inlet velocity is specified with a uniform distribution. The results are given in figure 4.5.

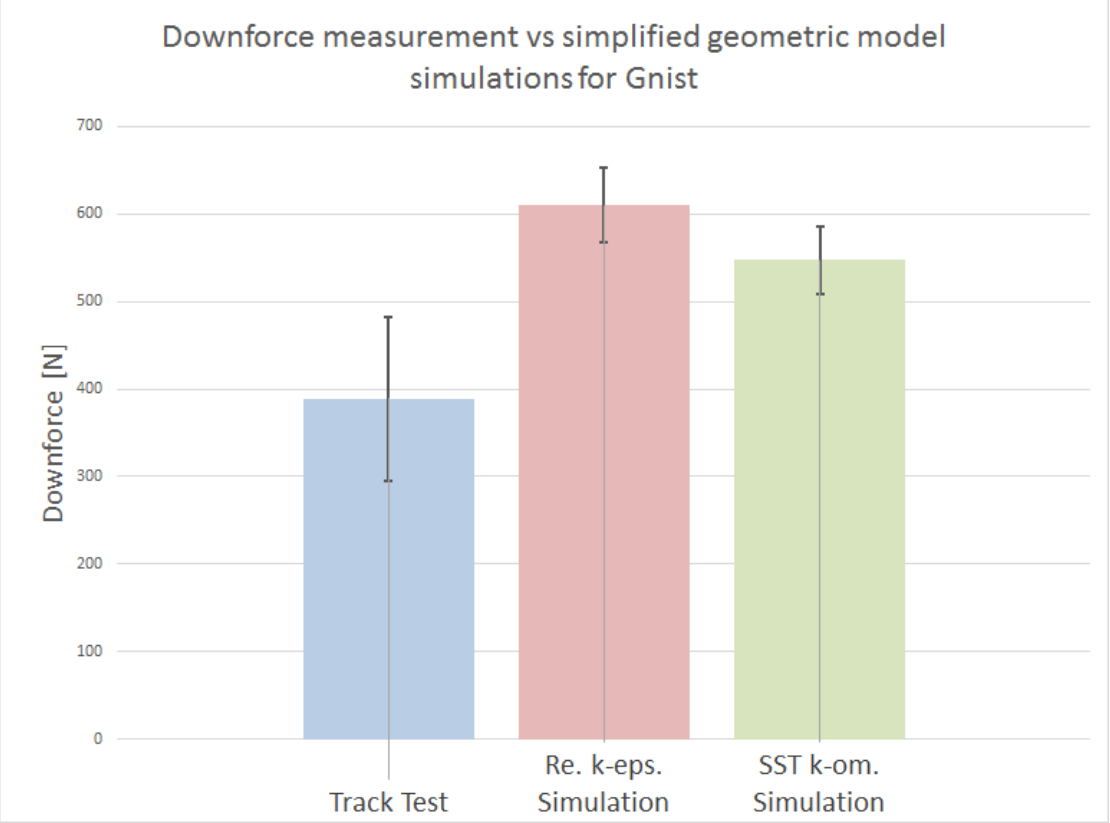

FIGURE 4.4: Measured and predicted lift for the real and simplified car model, respectively, for an estimated free stream velocity of 18.17 ms^{-1}.

4.4 Numerical results for momentum and forces on vehicle

Here the predicted aerodynamic forces and yaw, pitch and roll momentum for the vehicle model is presented. Note that because the environmental flow variables are the same for all cases the absolute values are given, for simplicity. Figures 4.6 to 4.8 presents the decomposed aerodynamic forces along the axes of the fixed global reference frame. Figures 4.9 to 4.11 presents the predicted aerodynamic moments generated about the vehicle's yaw, pitch and roll axes, respectively.

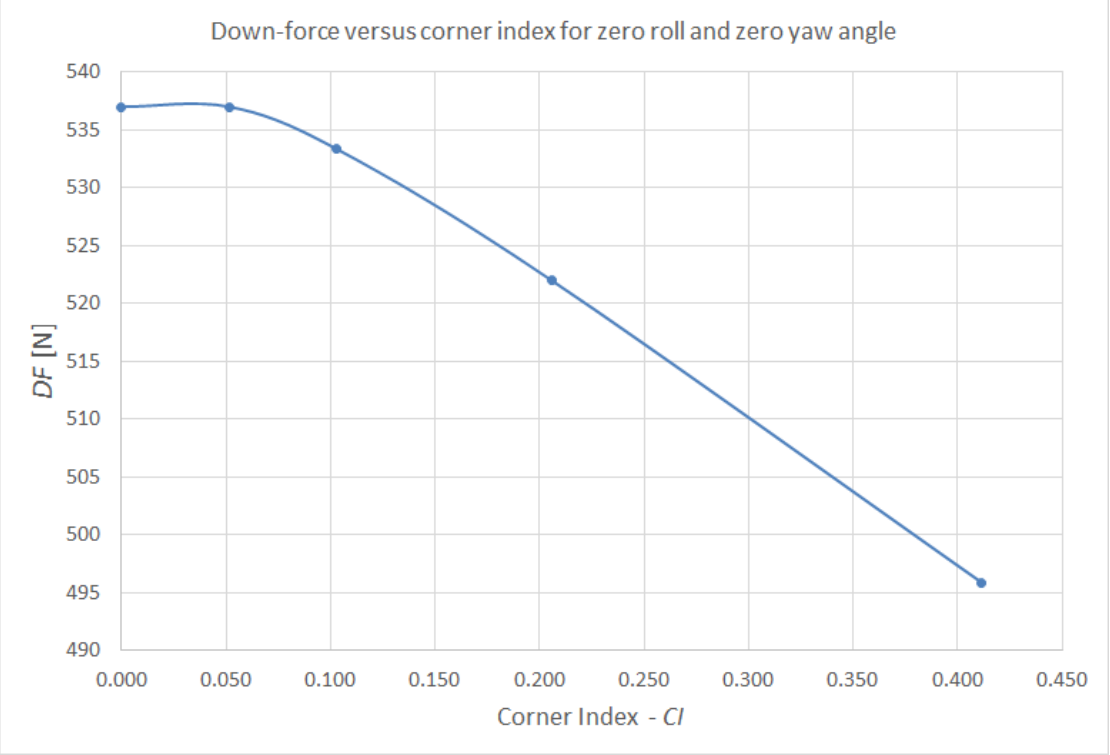

FIGURE 4.5: Generated DF as a function of vehicle CI. We observe that the rotational reference frame solution approaches the conventionally constructed straight line simulations, for increasing corner radii.

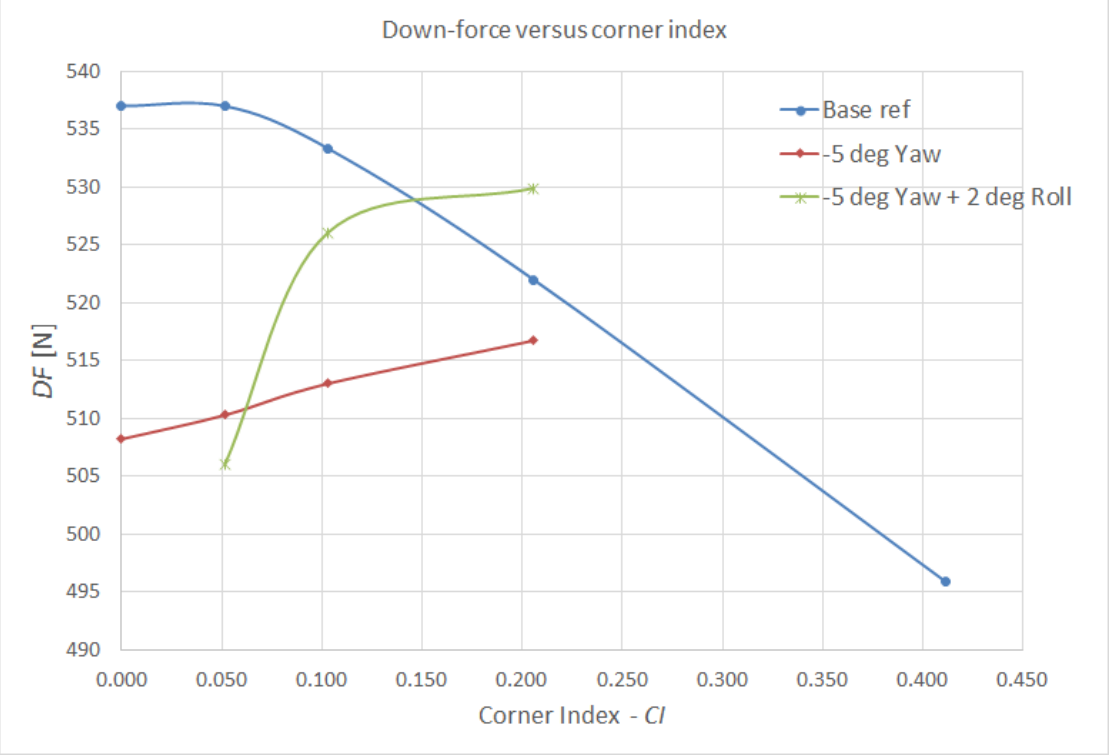

FIGURE 4.6: Generation of DF as a function of CI for three different car attitudes.

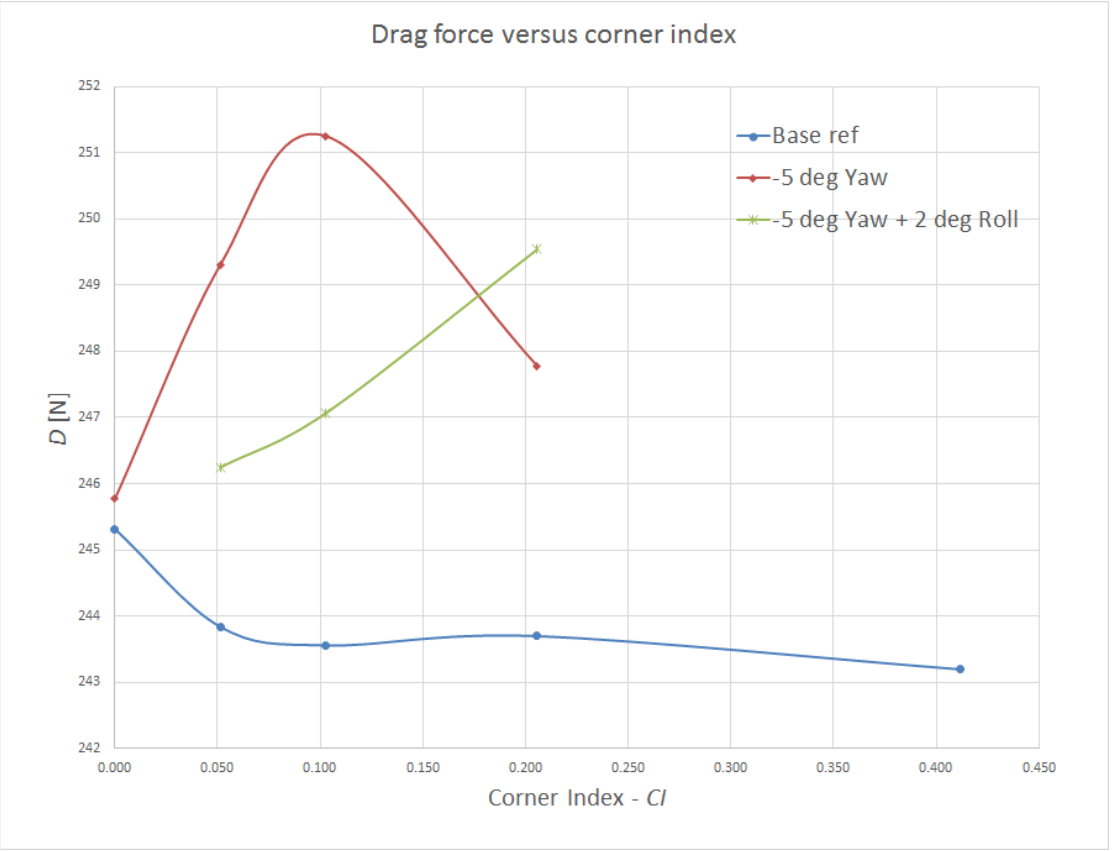

FIGURE 4.7: Generation of D as a function of CI for three different car attitudes.

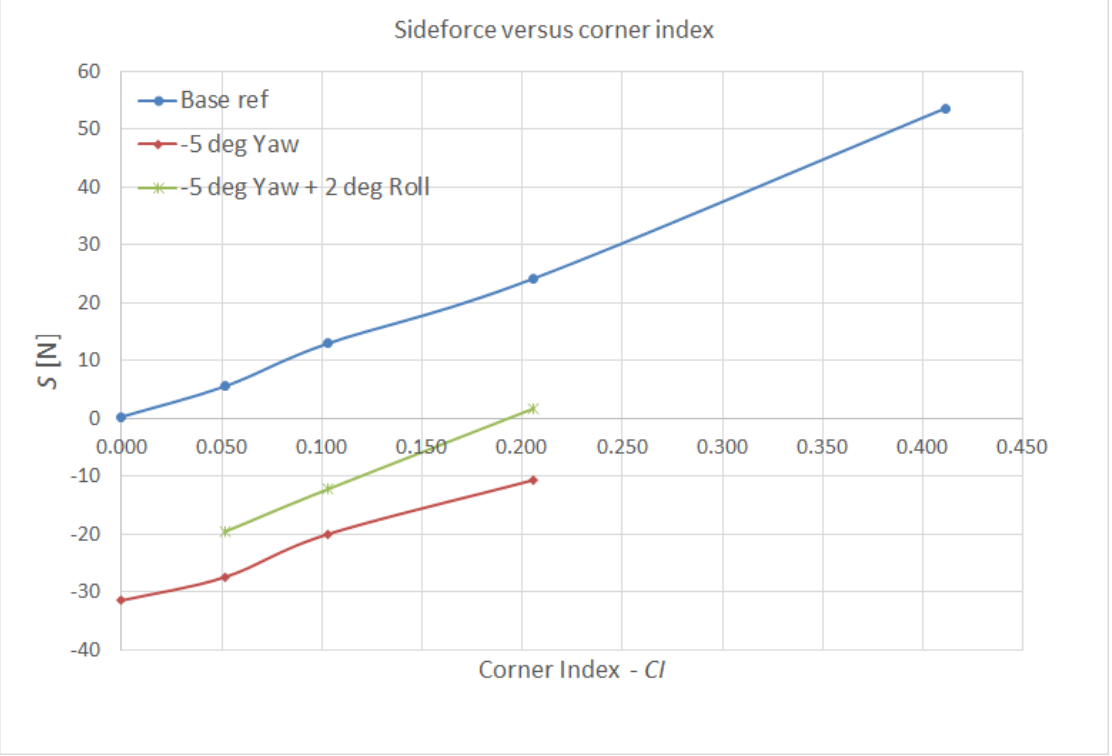

FIGURE 4.8: Generation of S as a function of CI for three different car attitudes.

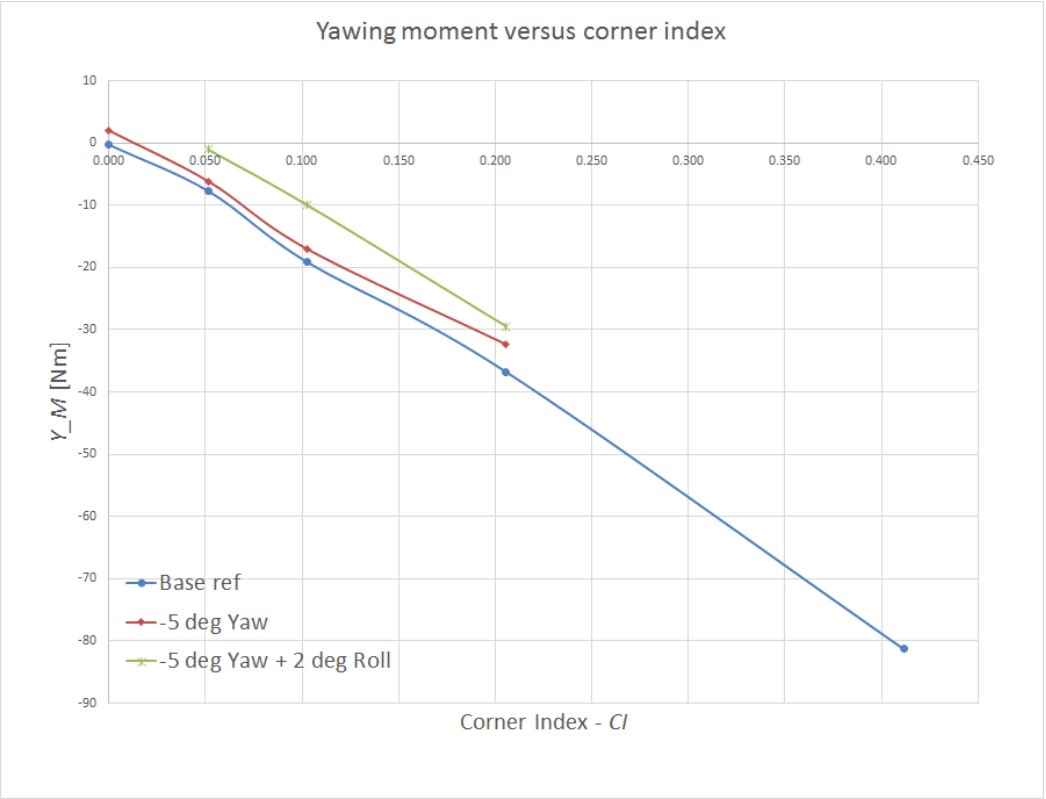

FIGURE 4.9: Predicted Y_m as a function of CI for three different car attitudes.

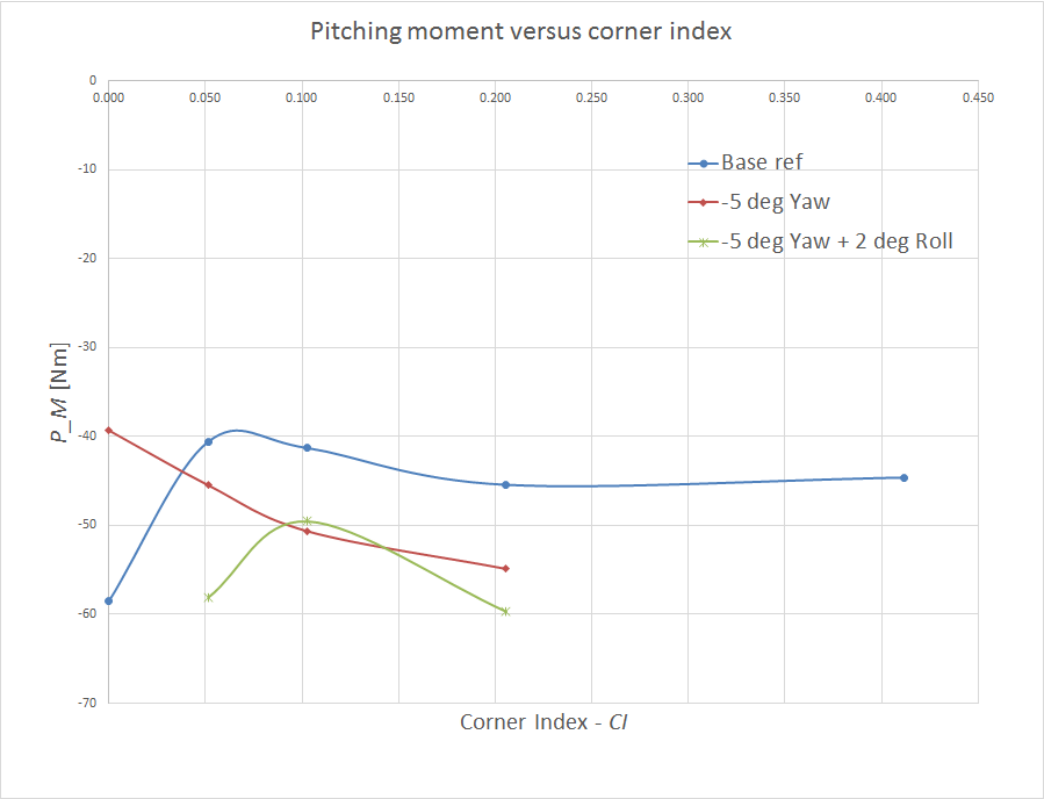

FIGURE 4.10: Predicted P_m as a function of CI for three different car attitudes

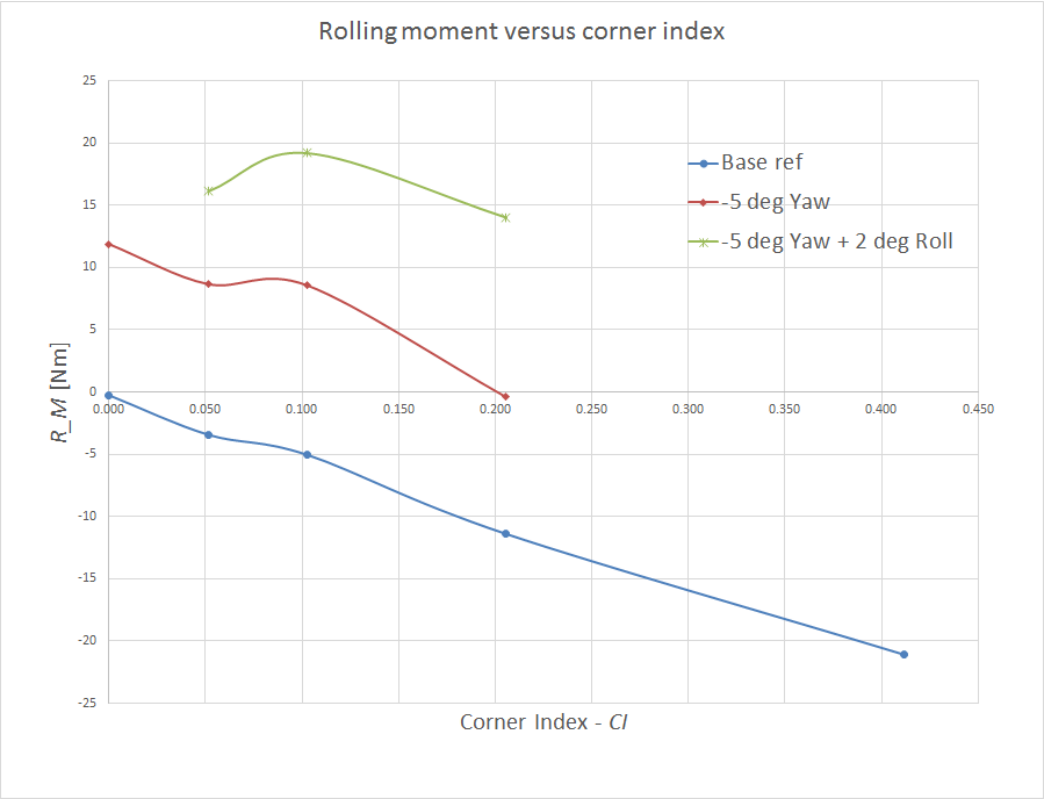

FIGURE 4.11: Predicted R_m as a function of CI for three different car attitudes

4.5 CFD visualizations

In figure 4.12 an overview of the car model with velocity and pressure planes can be seen. In figure 4.13-4.15 pressure surface plots for 3 different car configurations is presented.

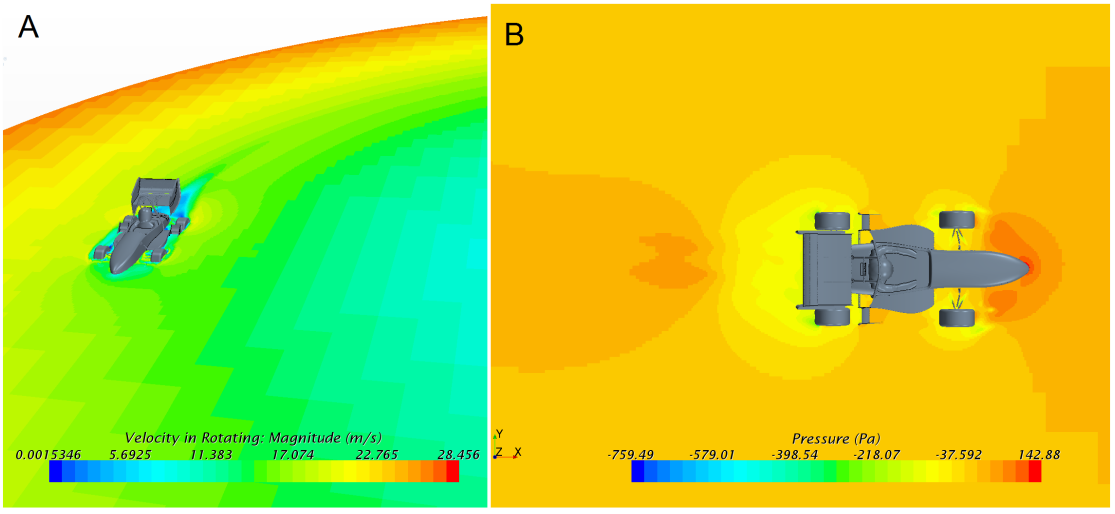

FIGURE 4.12: In A: Overview of the velocity field on a horizontal plane at the height of the wheel axles for a 14 m radius turn. In B: pressure distribution in the same plane as for A. Here with zero yaw and roll.

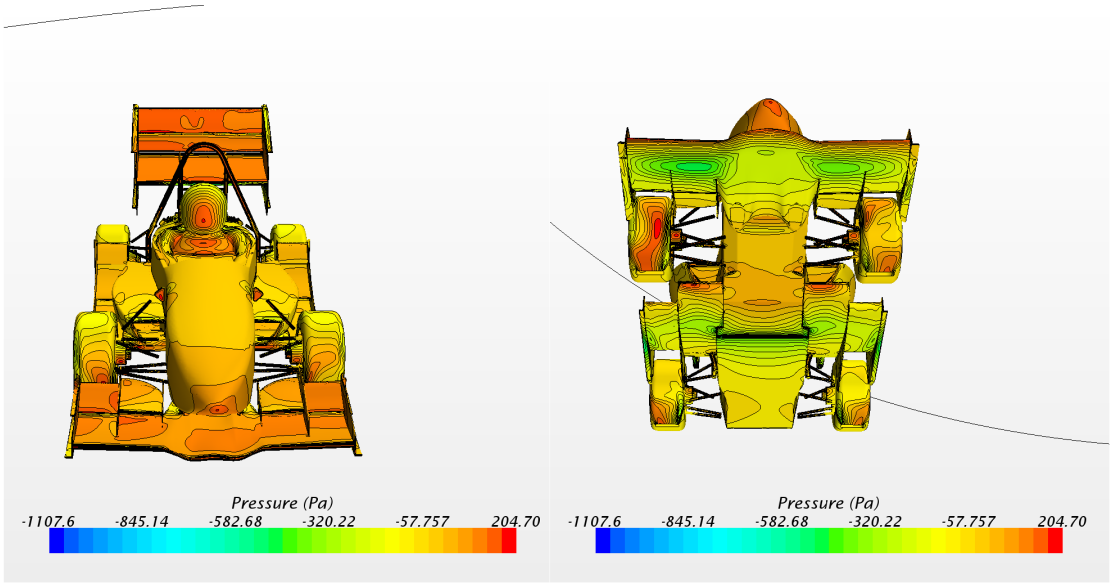

FIGURE 4.13: Vehicle surface pressure distributions for the case of a 14 m radius turn with zero roll and yaw.

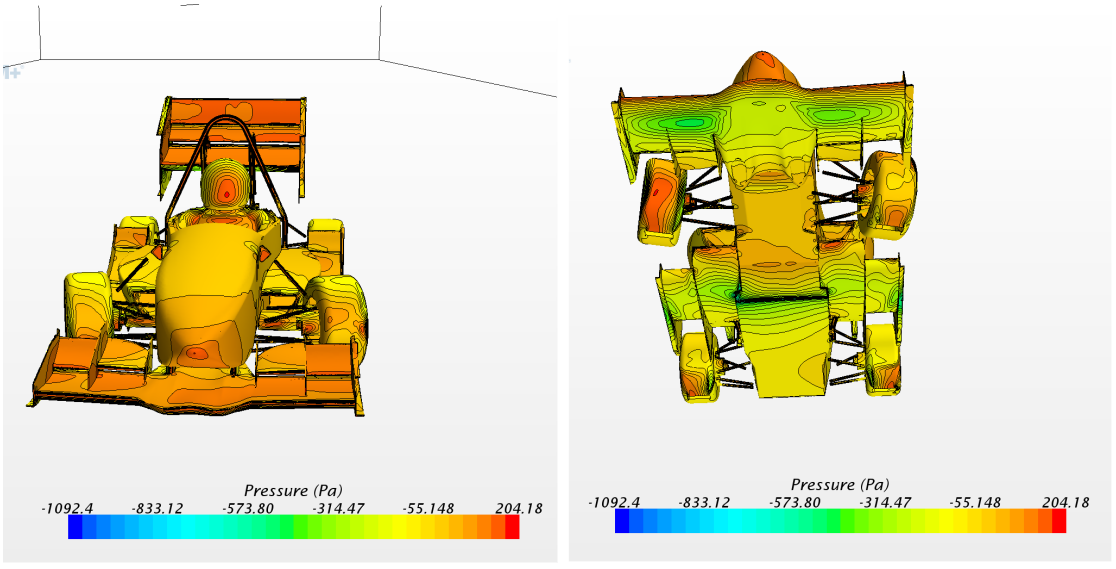

FIGURE 4.14: Vehicle surface pressure distributions for the case of a pure -5 deg yaw. Straight tunnel domain.

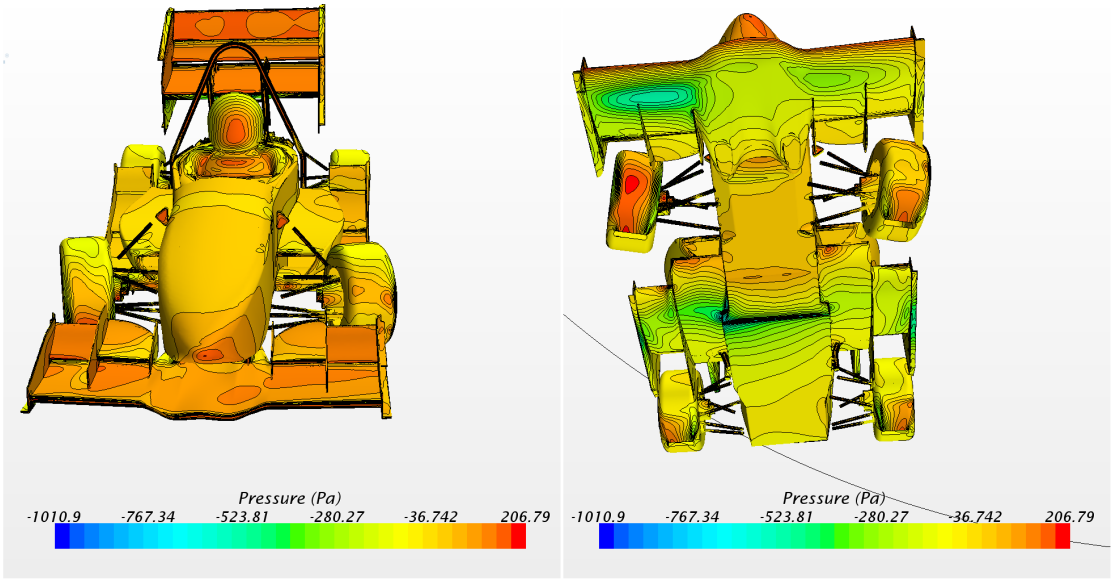

FIGURE 4.15: Surface pressure distribution for the case of a 14 m radius turn for a car with a -5 degree yaw, and 2 degree roll. Note the distinct increase in suction on the left side for the vehicle, as viewed from a reader's point of view.

Chapter 5

Discussion

5.1 Observartions from the single and 3 element wing validation test cases

For the case of the NRELs826, we note a tendency for the 2D simulations to under predict drag, with the exception of the Spalart-Allmaras turbulence model simulations. The 3D simulations using the Realizable $k - \varepsilon$ turbulence model agrees well with experimental data, but can bee seen to predict a slight delay in stall of the wing, with respect to experiments. For a full discussion, see [28].

In the case of the 3 element wing a good agreement between the predicted and measured lift and drag coefficients are observed. Very little degree of separation was predicted by the simulations, and this was supported by smoke visualization tests conducted in the wind tunnel. An photo from the test indicating attached trailing edge flow is included in the appendix.

5.2 Observations from the full car simulations and the track test results

As expected, we observe an over prediction of generated DF by the numerical simulations for the simplified car geometry, with respect to measurements, for an estimated free stream velocity of 18.17 ms^{-1}.

While the RANS type steady state simulations are widely used and validated for cases with little to mildly separated flows [31][32], problems arise when the turbulence models are used in cases with large areas of separation, which is typically the case for open wheel

race-cars [4]. In a separate article by the author [28], it was shown how the Realizable k-epsilion turbulence model can give a qualitatively reasonable picture of the stall condition of a single airfoil. However, the model can not be expected to predict the right scale of the wake, or downstream extent. This is related to the high degree of diffusivity in steady state RANS simulations, an effect that previous work have been concerned with, particularly in analysing stream wise vortexes for which Steinhoff proposed a vorticity confinement model [33]. As such, for as a complex case as an entire car, we cannot expect a high fidelity in the prediction in overall down-force and drag by the above mentioned CFD models. In this car model in particular, a lot (> 25 %) of the generated down force is designed and predicted by the simulations, to be generated by the under-body diffusers and side wings, working in ground proximity. Because these are situated directly downstream of the front tires, predicting the overall extent of the wake from the tires is important in predicting the flow conditions for lift generation for these devices. Further, because RANS simulations have been shown to under predict the stream wise extent and cross section of a wake [22, 34], we might expect an over prediction in the generated lift by the simulations compared to real life tests. This is exactly what we observe in the comparison between the track tests and the validation simulations.

From the damper displacements measurement on the separate wheels from the track tests, given in appendix A, we observe a 53% rear, and 47% front distribution of the total lift on the car. This is in good agreement with the distribution predicted predicted by the Realizable $k - \varepsilon$ simulation results, and supports the above argument that the a large portion of the deviation in the predicted versus real lift values is due to the difficulty in predicting the wake of the front tires and subsequently the flow around the car's side wings and under-body diffusers. The lift generated by these devices acts in a projected line close to the car's pitch axis, and will therefore have a much smaller impact on the overall vehicle balance relative to the impact from the front and rear wings.

On the day the track tests were conducted, steady wind speeds of roughly 2 m/s was measured by the nearby weather station at Værnes. Temperatures at the time of testing were around 17 C° with a relative humidity of 70 %. This, on itself, assuming a measured atmospheric pressure of 1 atmosphere at the test site[1] can only serve to increase the discrepancy between the measured forces and simulations of about 1.7%. This with respect to the modelled air density in the simulations of 1.17669 kgm^{-3}.

In the measured data, it was clear that a significant amount of the winds were aligned along the vehicles direction of heading, as the measured lift on the car varied consistently in the opposite direction of travel. Still, it is not unreasonable to estimate side-winds generating an effective yaw angle of around 7 degrees. From the measured lift on the

[1] Unfortunately, no weather statistics for the measured pressure in the area was found

rear wing of Vilje for different yaw angles conducted at NTNU's wind tunnel, this might account for roughly 10 % decrease in generated lift. Even so, the large variations in lift predicted by the simulation relative to the measured lift cannot be accounted for.

Without a proper assessment of the impacts of the simplification of the car model relative to the actual geometry and measurements of local turbulence at the test site, relative to the turbulence modelled, a conclusion cannot be made regarding the validation of the numerical approach. A further investigation is recommended for the case of the modelling approach of the car as a whole.

5.3 Comparison between straight line and curved domain simulations

From the results we observe that the overall generation of lift is effected negatively by both yaw angle and curvature of flow with respect to the car. Drag is not observed to be significantly affected. In accordance with [5], the increased rotation of flow creates a positive side force pushing the vehicle into the turn. However, simultaneously, a negative yawing moment is created, steering the vehicle out of the turn. We note that for the case of $CI = 0$, the 5 degree yaw creates a self aligning momentum about the yaw axis. This is likely due to the large rear wing end plates, working as a guiding fin for the car. The same concept is commonly implemented for race-cars driving on tracks with relatively small corner indexes compared to the case presented here [4]. It is interesting to note then, that as the corner index increases, the opposite happens, and the large surface areas of the wing end plates only serve to push the vehicle out of the turn. In terms of keeping the yaw momentum as neutral as possible then, formula student teams might want to thoroughly weigh the added DF from the end plates against the under steer momentum generated.

In the case of the car modelled with roll, we observe a relatively large change in momentum generated about the roll axis when going from a zero to a 2 degree roll angle. The effect is, as expected, self-enforcing, and a car beginning to roll out in a corner due to weight transfer will only be reinforced by aerodynamic momentum. The vehicle will continue to roll until a new equilibrium is found, which may be far out relative to the roll angle predicted from a purely vehicle kinematics point of view. Future aerodynamic teams may want to redesign the aerodynamic devices so that a roll angle will not create self-enforcing effect by positioning the wings differently on the ground effect curve.

Looking at the pressure distributions of the car for the different cases, we note that all cases of yaw and rotational flow shifts the stagnation pressure point towards the inside

of the car. This is the expected behaviour and agrees with the numerical yaw momenta predicted. We also note that in the curved flow simulations, the pressure distribution appear symmetrical along the car width at the mid-wheelbase position. This is as it should be, as this is the point where the flow is parallel to the car longitudinal direction, in the case of 0 degree yaw.

In all cases presented with surface pressure plots, a high pressure point builds up on the outside front tire. A front wing redesign might help ease the negative yaw moment generated.

Chapter 6

Conclusion

This study has considered different RANS turbulence models and found that with respect to reproducing flow effects and aerodynamic performance of relatively simple wing geometries, simulations with the Spalart-Allmaras, Realizable $k-\varepsilon$ and Menter SST $k-\omega$ turbulence models can all be said to give fair results as long as flow is largely attached to wing surfaces. Relatively large discrepancies arise when the turbulence models are asked to handle turbulent wakes in separated flows. This is in agreement with findings in the literature.

For the case of estimating the overall performance of the formula student race-car Gnist, a relatively large discrepancy was observed from estimates obtained with a simplified car geometry, with respect to measured forces on the vehicle out on track. It is believed that this is due in part to the simplification in the model geometry, and in part due to side winds present during track testing. A further investigation is suggested for future work.

In modelling cornering rotational flow around the car, a significant difference was found with respect to pure yaw angles sometimes used to model race cars in corners. Even for relatively large corner radii, or small corner indexes, modelling pure yaw angles would lead to opposing conclusions for the case assessing yaw moment on the car. This leads to the conclusion that for a Formula student vehicle, the better approach would be to model a cornering car by implementing a rotational reference frame motion in addition to setting the appropriate vehicle attitudes.

Bibliography

[1] S. Wordley and J. Saunders. Aerodynamics for formula SAE: A numerical, wind tunnel and on-track study. *SAE International Paper*, (2006-01-0808), 2006.

[2] P. Doddegowda, A. L. Bychkovsky, and A. R. George. Use of computational fluid dynamics for the design of formula SAE race car aerodynamics. *SAE paper*, (2006-01-0807), 2006.

[3] A. R. Hammond and R. G. J. Flay. Aerodynamic design of a formula sae race car. In *BBAA VI International Colloquiun on: Bluff Bodies Aerodynamics Applications*, Milano, Italy, July 2008.

[4] J. Katz. *Race Car Aerodynamics - Designing for speed.* Bentley Publishers, 1 edition, 1995.

[5] K. Watanabe and K. Matsuno. Moving computational domain method and its application to flow around a high-speed car passing through a hairpin curve. *Journal of computational science and technology*, 3(2):449–459, 2009.

[6] J. Keogh, G. Doig, S. Diasinos, and T. Barber. The influence of cornering on the vortical wake structures of an inverted wing. *Proc IMechE part D, Journal of Automobile Engineering*, (10):1–13, January 2015.

[7] H. K. Versteeg and W. Malalasekera. *An Introduction to Computational Fluid Dynamics.* Pearson Education, Harlow, 2 edition, 2007.

[8] P.J Roache. Quantification of uncertainty in computational fluid dynamics. *Annu. Rev. Fluid. Mech.*, 29:123–60, 1997.

[9] H. B. Pacejka. *Tyre and vehicle dynamics.* Elsevier, 2 edition, 2006.

[10] W. F. Milliken and D. L. Milliken. *Race Car Vehicle Dynamics.* SAE International, 1 edition, 1995.

[11] E. Cui and X. Zhang. Ground effect aerodynamics. *Encyclopedia of Aerospace Engineering*, pages 245–256, 2010.

[12] X. Zhang, W. Toet, and J. Zerihan. Ground effect aerodynamics of race cars. *Applied Mechanics Reviews*, 59:33–49, January 2006.

[13] G. Doig, T. J. Barber, and A. J. Neely. The influence of compressibility on the aerodynamics of an inverted wing in ground effect. *Journal of fluids engineering*, 133(061102-1), June 2011.

[14] J. H. Ferziger and M. Peric. *Computational Methods for Fluid Dynamics*. Springer, 3 edition, 2002.

[15] J. C. Tannehill, D. A. Anderson, and R. H. Pletcher. *Computational Fluid Mechanics and Heat Transfer*. Taylor & Francis, 2 edition, 1997.

[16] P. A. Thompson. *Compressible-Fluid Dynamics*. McGRAW-HILL, 1 edition, 1972.

[17] P. R. Spalart and S. R. Allmaras. A one-equation turbulence model for aerodynamic flows. In *30th AIAA Aerospace sciences meething and exhibit*, Reno, NV, U.S.A, January 1992.

[18] CD-adapco. *StarCCM+ user guide*. Code version 10.02.012.

[19] NASA Langley Research Center. Turbulence modelling resource; the spalart-allmaras turbulence model.

[20] T. Shih, W. W. Liou, A. Shabbir, Z. Yang, and J. Zhu. A new k-e eddy viscosity model for high reynolds number turbulent flows. *Computers Fluids*, 24(3):227–238, March 1995.

[21] F. R. Menter. Two-equation eddy-viscosity turbulence models for engineering applications. *AIAA Journal*, 32(8):1598–1605, August 1994.

[22] S. Diasinos, T. J. Barber, and G. Doig. The effects of simplifications on isolated wheel aerodynamics. *Journal of wind engineering and industrial aerodynamics*, 146: 90–101, June 2015.

[23] J. McManus and X. Zhang. A computational study of the flow around an isolated wheel in contact with the ground. *Journal of Fluids Engineering*, 128:520–530, May 2006.

[24] J. Keogh, G. Doig, and S. Diasinos. Flow compressibility effects around an open-wheel racing car. *Aeronautical Journal*, 118:1409–1431, December 2014.

[25] P. R. Spalart. Young-person's guide to detached-eddy simulation grids. Technical report, NASA, Langley Research Center, 2001.

[26] D. M. Somers. The s825 and s826 airfoils. Technical Report SR-500-36344, NREL, 2005.

[27] N. Y. Aksnes. Performance characteristics of the nrel s826 airfoil. Master's thesis, NTNU, Trondheim, Norway, 2015.

[28] K. F. Sagmo, L. Sætran, and J. Bartl. Numerical simulations of the NREL S826 airfoil. *J. Phys.: Conf. Series*, September 2016.

[29] B. W. Omholt. Direct yaw moment, traction and power limit control of a four wheel independent drive electric (4wid-ev) formula student race car. Master's thesis, NTNU, Trondheim, Norway, August 2016.

[30] H. Sarlak, R. Mikkelsen, S. Sarmast, and J. N. Srensen. *J. Phys.: Conf. Series*, 524, 2014.

[31] S. C. Cakmakcioglu, I. O. Sert, O. Tugluk, and N. Sezer-Uzol. 2-d and 3-d cfd investigation of NREL S826 airfoil at low reynolds numbers. *J. Phys.: Conf. Series*, 524, 2014.

[32] K. Ren, J. Hu, X. Xiong, L. Zhang, and J. Wei. Validation of turbulence models in star-ccm+ by n.a.c.a. 23012 airfoil characteristics. In *ASEE Northeast Section Conference*, Bridgeport, CT, April 2009.

[33] J. Steinhoff, N. Lynn, and L. Wang. Computation of high reynolds number flows using vorticity confinement: I. formulation. *UTSI preprint*, 2005.

[34] M. Manolesos, G. Papadakis, and S Voutsinas. An experimental and numerical investigation on the formation of stall-cells on airfoils. *J. Phys.: Conf. Series*, 555, 2014.

Appendix A

Damper Measurements

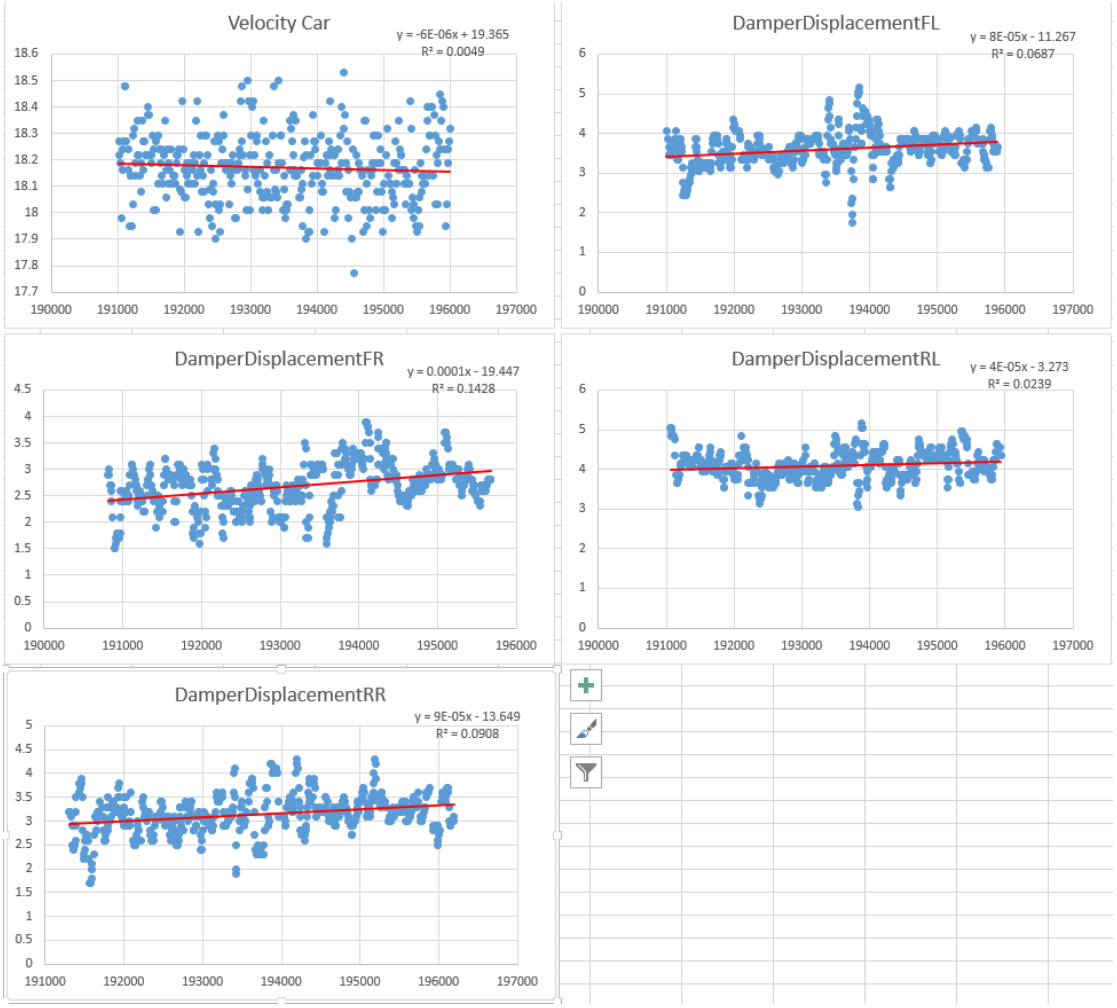

FIGURE A.1: Optical sensor measurements of car velocity along with damper displacement measurements for the front left (FL), front right (FR), rear left (RL) and rear right (RR) wheels, as viewed from the driver. Run 1.

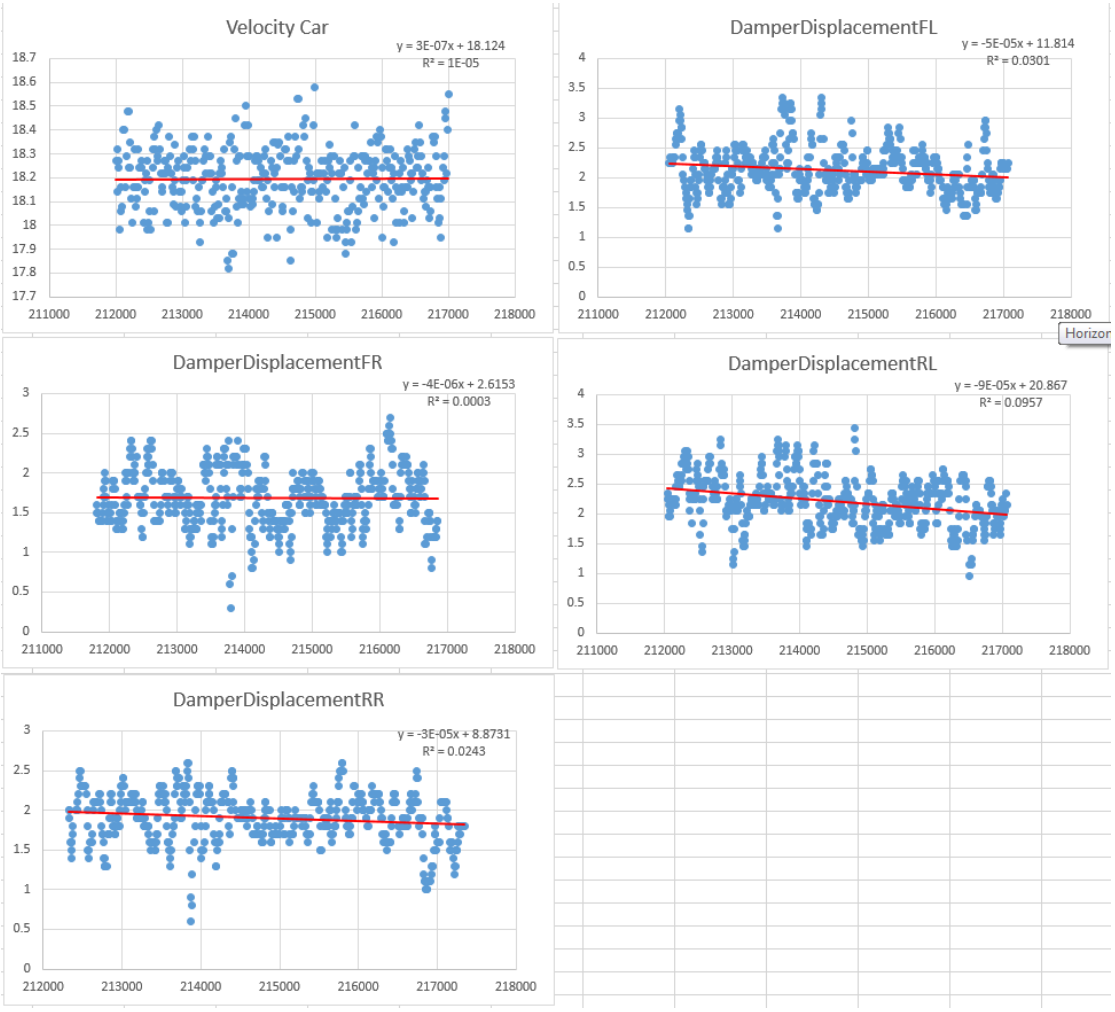

FIGURE A.2: Optical sensor measurements of car velocity along with damper displacement measurements for the front left (FL), front right (FR), rear left (RL) and rear right (RR) wheels, as viewed from the driver. Run 2.

FIGURE A.3: Optical sensor measurements of car velocity along with damper displacement measurements for the front left (FL), front right (FR), rear left (RL) and rear right (RR) wheels, as viewed from the driver. Run 3.

FIGURE A.4: Optical sensor measurements of car velocity along with damper displacement measurements for the front left (FL), front right (FR), rear left (RL) and rear right (RR) wheels, as viewed from the driver. Run 4.

FIGURE A.5: Optical sensor measurements of car velocity along with damper displacement measurements for the front left (FL), front right (FR), rear left (RL) and rear right (RR) wheels, as viewed from the driver. Run 5.

FIGURE A.6: Optical sensor measurements of car velocity along with damper displacement measurements for the front left (FL), front right (FR), rear left (RL) and rear right (RR) wheels, as viewed from the driver. Run 6.

Appendix B

Measurments of lift for the rear wing of Vilje

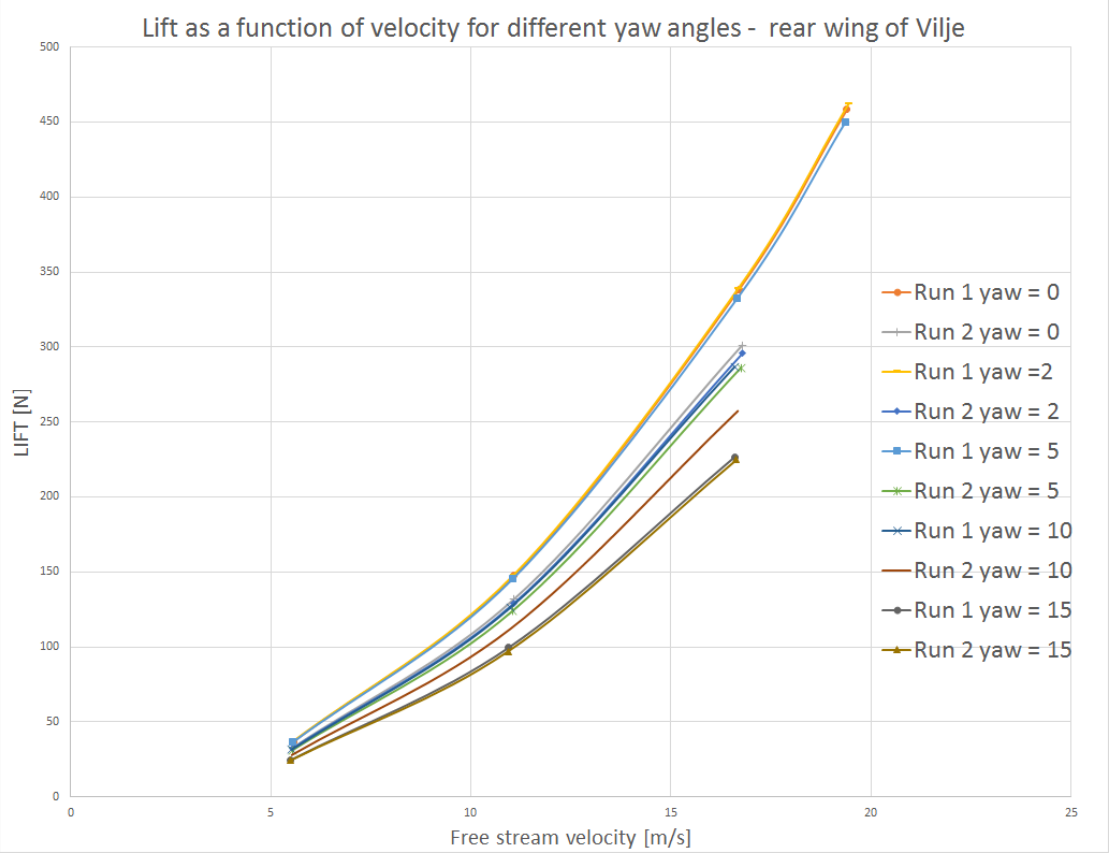

FIGURE B.1: Raw measurements of the generated negative lift for the 3 element wing at different yaw angles, as a function of velocity. Overall, yaw is seen to be detrimental to the generation of lift, and around a 13 % deficit is observed for a yaw angle of 10 degrees.

Appendix C

Wind tunnel smoke Visualization test for the the rear wing of Vilje

FIGURE C.1: A photo taken during the smoke visualization test conducted in the wind tunnel at NTNU for the rear wing of Vilje. Photo courtesy of Revolve NTNU.

Appendix D

Example Numerical Residuals

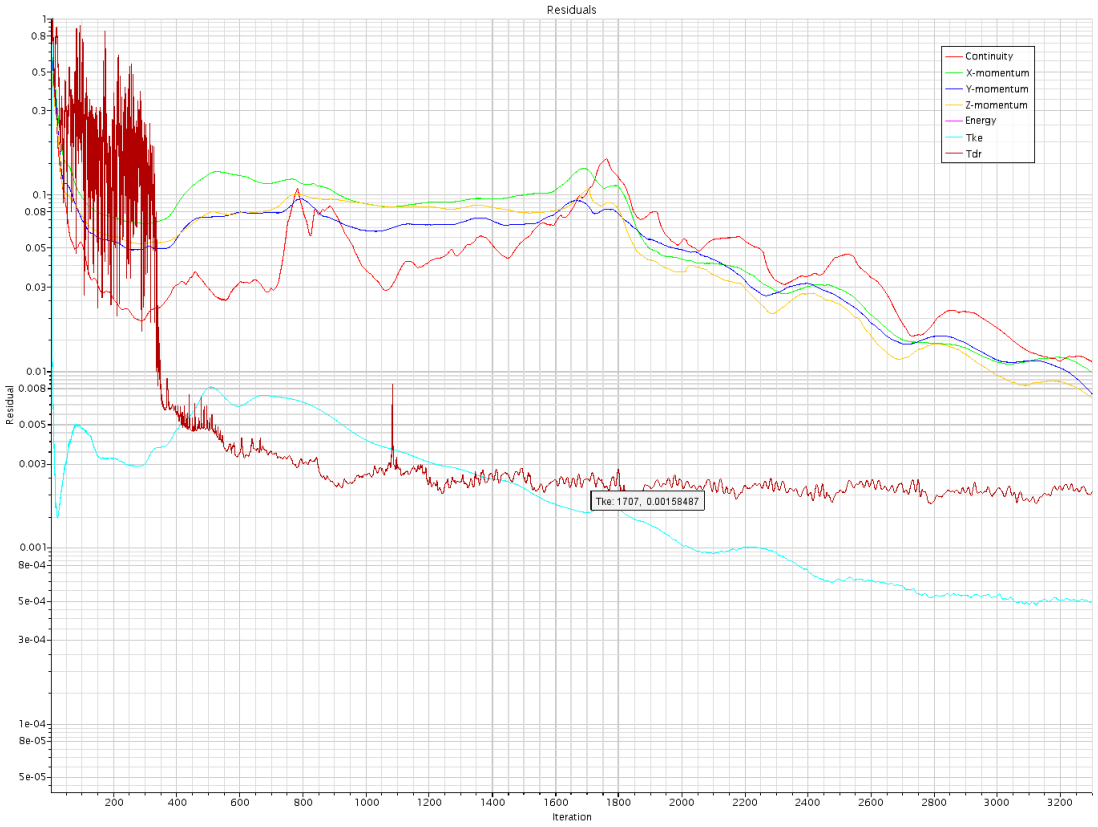

FIGURE D.1: Relative numerical residuals for a full car simulation using the Realizable $k-\varepsilon$ turbulence model. Here for a cornering simulation with a radius of 56 metres.